



A highly accurate boundary integral equation method for surfactant-laden drops in 3D



Chiara Sorgentone*, Anna-Karin Tornberg

KTH Mathematics, Linné Flow Centre/Swedish e-Science Research Centre, 10044 Stockholm, Sweden

ARTICLE INFO

Article history:

Received 6 July 2017

Received in revised form 15 January 2018

Accepted 18 January 2018

Available online 31 January 2018

Keywords:

Boundary integral method

Stokes flow

Surfactant

Spherical harmonics

ABSTRACT

The presence of surfactants alters the dynamics of viscous drops immersed in an ambient viscous fluid. This is specifically true at small scales, such as in applications of droplet based microfluidics, where the interface dynamics become of increased importance. At such small scales, viscous forces dominate and inertial effects are often negligible. Considering Stokes flow, a numerical method based on a boundary integral formulation is presented for simulating 3D drops covered by an insoluble surfactant. The method is able to simulate drops with different viscosities and close interactions, automatically controlling the time step size and maintaining high accuracy also when substantial drop deformation appears. To achieve this, the drop surfaces as well as the surfactant concentration on each surface are represented by spherical harmonics expansions. A novel reparameterization method is introduced to ensure a high-quality representation of the drops also under deformation, specialized quadrature methods for singular and nearly singular integrals that appear in the formulation are evoked and the adaptive time stepping scheme for the coupled drop and surfactant evolution is designed with a preconditioned implicit treatment of the surfactant diffusion.

© 2018 Elsevier Inc. All rights reserved.

Introduction

Micro-fluidics, or fluid mechanics at small scales, is an expanding research area. Droplet-based microfluidics is a sub-category of microfluidics where tiny (e.g. picoliter sized) droplets are used as the equivalent of “test tubes”, offering the possibility of high throughput experiments that enhance the speed of chemical and biological assays [49,43]. Owing to the small scales, viscous forces dominate and inertial effects are often negligible. Due to the large surface to volume ratio, the importance of interface dynamics becomes pronounced. As water droplets are dispersed in oil, they are stabilized by a powerful surfactant preventing them from coalescing. These surface active agents are compounds that lower the surface tension between liquids; they are widely used in engineering applications, in pharmaceuticals, foods and petroleum industries [27, 45]. Surfactants can also be found in e.g. detergents, emulsifiers, paints, adhesives, inks and alveoli.

The surfactant concentration can be modeled with a time dependent differential equation defined on the moving and deforming interface, coupled with the Stokes equation for the evolution of the droplets through a non-linear equation of state relating the surface tension to the surfactant concentration. There are two competing processes governing the effect of surfactants on drop deformation [18]: surfactant dilution and surfactant convection. The first one is due to deformation of the drop from a spherical shape, which causes an increase of total surface area and a consequent decrease of surfactant

* Corresponding author.

E-mail addresses: sorgentone@kth.se (C. Sorgentone), akto@kth.se (A.-K. Tornberg).

concentration, hence smaller deformation. The fluid flow will however typically cause surfactant convection that tends to increase the concentration at the tips of the drop, resulting in an increasing drop deformation.

There are several studies of drop behavior without surfactants (see [47,60,55] for a summary), but the behavior of the surfactant-covered droplets has been much less studied, especially in 3D. In 2D there is a number of papers for insoluble surfactants, see e.g. [48,57,28]. For soluble surfactants where the surfactant is assumed to have a concentration also in one of the fluid phases, there are fewer studies, see e.g. [29,56]. For the 3D problem, one of the earlier studies is due to Li and Pozrikidis [31] in 1997, followed by another paper of Yon and Pozrikidis [59], where the drop deformation in shear flow is studied for the special case of viscosity ratio equal to one (same viscosity inside and outside the drop). Arbitrary viscosity ratio has been considered later on: Bazhlekov et al. presented a numerical investigation of the effect of insoluble surfactants on drop deformation and break up [8] and in [18] Feigl et al. presented a study of the same problem combining numerical simulations with experiments on droplets. In all of the mentioned cases a boundary integral formulation has been used. More recently, Teigen et al. proposed a diffuse-interface method [50], and Muraduglo and Tryggvason [35] a front-tracking method for drops with soluble surfactant.

These micro-fluidic problems are very challenging to simulate accurately and efficiently, especially in three dimensions. The geometry is time-dependent due to the motion and deformation of the drops, surface tension forces induce jumps in pressure and velocity gradients across the drop surfaces, and the presence of surfactants require the solution of a time dependent PDE on each deforming drop surface. Using grid-based methods to solve the Stokes (or Navier–Stokes) equations, the computational grid/mesh is typically not required to conform to the drop interfaces that could be kept track of by front-tracking [35], a level set method [57] or a phase field function with a diffuse interface layer as in [50]. The singular surface tension forces are commonly regularized onto the grid, yielding only first order accuracy close to the interface as measured in the resolution of the volume grid. Recent advances have been made to develop so-called cut cell methods to increase this accuracy to second order, see e.g. [24] and the references therein.

For the case of Stokes equations a boundary integral equation can be formulated. This is a sharp interface formulation for which the above mentioned issues are avoided – there is no underlying volume grid to couple to, jumps in solutions are naturally taken care of, and viscosity ratios between fluids enter only in coefficients of the equations. The formulation contains integrals only over the fluid–fluid interfaces and possibly external boundaries, reducing the dimension of the problem, and hence the number of unknowns in the discretized problem.

There are many discretization choices to be made for a boundary integral formulation, including how the drop surfaces should be represented and how the integrals in the equation should be evaluated. The integrals contain Green's functions for Stokes equations, which are singular but integrable when integrating over a drop surface for an evaluation point at that same surface, and nearly singular for an evaluation point on a drop surface nearby. Evaluating such integrals require special techniques.

One common way to discretize a surface is to use a triangulated surface [59,62]. We have chosen to use a higher order representation in terms of a parameterization of the surface, expressed as a spherical harmonics expansion with vector valued coefficients for the three drop coordinates. This has earlier been used e.g. for the simulation of vesicles and blood cells in Stokes flow [41,53,61]. An expansion of order p corresponds to $O(p^2)$ discrete points on the surface, and a discrete spherical harmonics transform can be used to compute the coefficients from the coordinates of these points. To evaluate the singular integrals mentioned above, we use a method that yields exponential convergence in p [22,53]. For the case of close interactions and hence nearly singular integrals, we adapt and optimize a procedure first presented by Ying et al. [58] to our problem. The errors can be kept at a very low level also here, if parameters are chosen appropriately.

When a drop moves and deforms, the point distribution will in general be distorted, and the surface needs to be reparameterized. The optimal spherical harmonics representation is the one that describes the surface using a set of expansion coefficients with the fastest decay with p , corresponding to a specific set of discrete points on the surface. The reparameterization procedure should yield a distribution close to optimal, and conserve the volume and surface area of the drop. In addition, it needs to yield a new parameterization for the surfactant concentration, that is also represented using a spherical harmonics expansion. The reparameterization procedure introduced by Veerapaneni et al. in [53] sets a nice framework which we have used to design a novel reparameterization technique that meets our requirements regarding volume/surface area conservation and reparameterization of the surfactant representation.

An adaptive time-stepping scheme is used to couple together the drop and the surfactant evolution. It uses an implicit treatment for the diffusive term in the surfactant equation, which reduces the CFL condition to first order. To make this implicit solver efficient also for large diffusion coefficients, a new preconditioner is introduced.

In total, the Boundary Integral Method (BIM) for 3D drops covered by an insoluble surfactant that we present here is able to handle drops with different viscosities and close interactions maintaining high accuracy even when strong deformations appears, automatically controlling the time stepping size.

The paper is organized as follows: in Section 1 we introduce the model, the boundary integral formulation and the Galerkin method used to solve the discrete system. In Section 2 we discuss the numerical integration with special attention to singular and nearly singular integrals. A study and comparison of different time-stepping schemes coupling together the drop and the surfactant evolution is presented in Section 3, where we also introduce the new preconditioner for the surfactant equation. The new reparameterization procedure is explained in Section 4 and numerical experiments for both clean and surfactant-covered drops are presented in Section 5, where we validate our method against numerical and experimen-

Table 1
List of symbols.

Symbol	Definition
Δ_γ	Surface Laplacian
∇_γ	Surface gradient
γ^*	Union of all drop surfaces $\bigcup_i \gamma_i$
μ_0	Viscosity of the ambient fluid
μ_i	Viscosity of the fluid inside the i -th drop
λ_i	The viscosity contrast $\frac{\mu_i}{\mu_0}$
\mathbf{u}	Interfacial velocity
\mathbf{u}_∞	Far field velocity
\mathbf{u}_γ	Tangential component of the interfacial velocity
\mathbf{u}_n	Normal component of the interfacial velocity
P	Pressure
σ	Dimensionless interfacial tension
Γ	Dimensionless surfactant concentration
Pe	Péclet number

Table 2
List of geometrical quantities.

Symbol	Definition	Symbol	Definition
E	$\mathbf{x}_\phi \cdot \mathbf{x}_\phi$	L	$\mathbf{x}_{\phi\phi} \cdot \mathbf{n}$
F	$\mathbf{x}_\phi \cdot \mathbf{x}_\theta$	M	$\mathbf{x}_{\phi\theta} \cdot \mathbf{n}$
G	$\mathbf{x}_\theta \cdot \mathbf{x}_\theta$	N	$\mathbf{x}_{\theta\theta} \cdot \mathbf{n}$
W	$\sqrt{EG - F^2}$	H	$\frac{1}{2} \frac{EN - 2FM + GL}{W^2}$, mean curvature
\mathbf{n}	$\frac{\mathbf{x}_\phi \times \mathbf{x}_\theta}{W}$, unit normal	K	$\frac{LN - M^2}{W^2}$, Gaussian curvature

tal results and where we also show the effect of surfactant in very near interaction of two drops. Conclusions and future perspectives are given in the last section.

1. Mathematical formulation

We consider N drops immersed in a liquid with different viscosity. The Stokes equations read

$$\begin{cases} -\mu_i \Delta \mathbf{u}(\mathbf{x}) + \nabla P(\mathbf{x}) = 0 \\ \nabla \cdot \mathbf{u}(\mathbf{x}) = 0 \\ \mathbf{u}(\mathbf{x}) \rightarrow \mathbf{u}_\infty(\mathbf{x}) \text{ as } |\mathbf{x}| \rightarrow \infty \end{cases} \quad (1)$$

for every \mathbf{x} inside the i -th drop ($i = 1, \dots, N$) or in the exterior region ($i = 0$), where \mathbf{u} is the fluid velocity, P is the pressure and μ_i is the viscosity (see [Tables 1 and 2](#)).

Let $\gamma^* = \bigcup_i \gamma_i$ denote the union of all drop surfaces/interfaces. There is a jump condition at γ^* that is given by

$$[[T\mathbf{n}]] = \mathbf{f}(\mathbf{x}) \quad (2)$$

where $T = -PI + \mu(\nabla \mathbf{u} + \nabla \mathbf{u}^T)$ is the Cauchy stress tensor, $[[\cdot]]$ denotes the jump across the interface and $\mathbf{f} = 2\sigma(\mathbf{x})H(\mathbf{x})\mathbf{n}(\mathbf{x}) - \nabla_\gamma(\sigma)$ is the interfacial force, with \mathbf{n} being the outward pointing unit normal and σ the interfacial tension. The evolution of the interfaces is given by

$$\frac{d\mathbf{x}}{dt} = \mathbf{u}(\mathbf{x}), \text{ for all } \mathbf{x} \in \gamma^*. \quad (3)$$

Letting a , σ_0 and μ_0 be, respectively, the radius of an undeformed spherical droplet, the interfacial tension of the clean interface and the viscosity of the ambient fluid, we can non-dimensionalize by taking the characteristic length to be a , the characteristic velocity to be $U = \frac{\sigma_0}{\mu_0}$ and the characteristic time $T = \frac{a\mu_0}{\sigma_0}$. Using the corresponding non-dimensionalized variables, equations (1)–(2) can be reformulated as a boundary integral equation [38]. For all $\mathbf{x}_0 \in \gamma_i$ ($i = 1, \dots, N$),

$$\begin{aligned} (\lambda_i + 1)\mathbf{u}(\mathbf{x}_0) = & 2\mathbf{u}_\infty(\mathbf{x}_0) - \sum_{j=1}^N \left(\frac{1}{4\pi} \int_{\gamma_j} \mathbf{f}(\mathbf{x}) \cdot G(\mathbf{x}_0, \mathbf{x}) d\mathbf{s}(\mathbf{x}) \right) \\ & + \sum_{j=1}^N \left(\frac{\lambda_j - 1}{4\pi} \int_{\gamma_j} \mathbf{u}(\mathbf{x}) \cdot T(\mathbf{x}_0, \mathbf{x}) \cdot \mathbf{n}(\mathbf{x}) d\mathbf{s}(\mathbf{x}) \right), \end{aligned} \quad (4)$$

where $\lambda_i = \frac{\mu_i}{\mu_0}$ denotes the viscosity contrast of the i -th drop. The tensors G and T are the Stokeslet and the Stresslet,

$$G(\mathbf{x}_0, \mathbf{x}) = I/r + \hat{\mathbf{x}}\hat{\mathbf{x}}/r^3, \quad T(\mathbf{x}_0, \mathbf{x}) = -6\hat{\mathbf{x}}\hat{\mathbf{x}}\hat{\mathbf{x}}/r^5,$$

where $\hat{\mathbf{x}} = \mathbf{x}_0 - \mathbf{x}$ and $r = |\hat{\mathbf{x}}|$. The limit to the boundary has been taken in (4) and the integrals are to be understood as principal value integrals. Using Eq. (4), we solve for the velocity of the drop surfaces, whereafter the drop evolution can be computed. The velocity can be evaluated anywhere in the domain whenever it is wanted (see [38] for details) but is not needed to determine the drop evolution. The velocity field is continuous across the interfaces γ_i , but its gradient and the pressure are not.

The evolution of the drops is affected by the presence of insoluble surfactant through a modified surface tension force. The equation governing the evolution of the surfactant concentration Γ is a convection–diffusion equation which can be derived stating the conservation of surfactant mass [46]; it is given in dimensionless terms by [46,8],

$$\frac{\partial \Gamma}{\partial t} + \nabla_{\gamma} \cdot (\Gamma \mathbf{u}_{\gamma}) - \frac{1}{Pe} \nabla_{\gamma}^2 \Gamma + 2K(\mathbf{x})\Gamma(\mathbf{u} \cdot \mathbf{n}) = 0, \quad (5)$$

where $Pe = \frac{a\sigma_0}{\mu_0 D_S}$ is the Péclet number, with D_S being the surface diffusivity. The interfacial tension is related to the surfactant concentration by the equation of state. Different equations of state can be used [37], we will use the Szyszkowski equation (also called Langmuir equation of state) which in dimensionless form is given by

$$\sigma(\Gamma) = 1 + E \ln(1 - x_s \Gamma) \quad (6)$$

where E is the elasticity number and x_s is the surface coverage, $0 \leq x_s \leq 1$. Equations (5)–(6) were non-dimensionalized by the characteristic velocity U , characteristic time T and the surfactant concentration Γ_{eq} for the same amount of surfactant uniformly distributed over a spherical drop with the same volume [8].

1.1. Surface representation

Assuming the surface γ_i of each drop to be smooth and of spherical topology, we will use a spherical harmonics expansion to represent it. Let $\mathbf{x} : U \rightarrow \gamma_i$ be a parametrization of γ_i , where the domain U is a rectangle $\{(\theta, \phi) : \theta \in [0, \pi], \phi \in [0, 2\pi]\}$. A scalar spherical harmonic function of degree n and order m is given by

$$Y_n^m(\theta, \phi) = \sqrt{\frac{2n+1}{4\pi} \frac{(n-m)!}{(n+m)!}} P_n^m(\cos(\theta)) e^{im\phi}, \quad -n \leq m \leq n, \quad (7)$$

where the associated Legendre function is defined by

$$P_n^m(x) = (-1)^m (1-x^2)^{m/2} \frac{d^m}{dx^m} P_n(x), \quad m \geq 0, \quad (8)$$

and

$$P_n^{-m}(x) = (-1)^m \frac{(n-m)!}{(n+m)!} P_n^m(x), \quad m \geq 0, \quad (9)$$

where P_n is the Legendre polynomial of degree n ,

$$P_n(x) = (2^n n!)^{-1} \frac{d^n}{dx^n} [(x^2 - 1)^n]. \quad (10)$$

Let $f : \mathbb{S}^2 \rightarrow \mathbb{R}$ be a square-integrable function. It can be expanded in terms of spherical harmonics as

$$f(\theta, \phi) = \sum_{n=0}^{\infty} \sum_{m=-n}^n f_n^m Y_n^m(\theta, \phi) \quad (11)$$

where the coefficients f_n^m are the moments of the expansion,

$$f_n^m = (f, Y_n^m) = \int_0^{\pi} \int_0^{2\pi} f(\theta, \phi) \overline{Y_n^m(\theta, \phi)} \sin \theta d\theta d\phi. \quad (12)$$

We truncate the spherical harmonic expansion at some degree p ,

$$f_p(\theta, \phi) = \sum_{n=0}^p \sum_{m=-n}^n f_n^m Y_n^m(\theta, \phi). \quad (13)$$

A drop surface will be represented by three such truncated scalar expansions,

$$\mathbf{x}(\theta, \phi) = [x(\theta, \phi), y(\theta, \phi), z(\theta, \phi)] = \sum_{n=0}^p \sum_{m=-n}^n [x_n^m, y_n^m, z_n^m] Y_n^m(\theta, \phi) \quad (14)$$

where we have omitted the subscript p and also the index of the drop for simplicity. We will denote by $\mathbf{x}_n^m = [x_n^m, y_n^m, z_n^m]$ the spherical harmonics coefficients vector. The surfactant concentration corresponding to this drop surface is similarly represented as

$$\Gamma(\theta, \phi) = \sum_{n=0}^p \sum_{m=-n}^n \Gamma_n^m Y_n^m(\theta, \phi). \quad (15)$$

We will compute derivatives of functions using analytical formulas in the spectral domain, see [Appendix A](#).

1.2. Galerkin formulation

To solve the integral equation (4), the evolution equation (3) and the surfactant equation (5), we use a Galerkin formulation as suggested in [41], where a similar approach is used to simulate the flow of vesicles. Let \mathbb{S}^2 denote the unit sphere and (\cdot, \cdot) the inner product $(f, Y_{nm}) = \int_{\mathbb{S}^2} f \overline{Y_{nm}} ds$, then the Galerkin method seeks the solution to the original system by

$$(\lambda_i + 1)(\mathbf{u}, Y_{nm}) = (\mathbf{u}^\infty, Y_{nm}) + \sum_{j=1}^N [(S_j[\mathbf{f}], Y_{nm}) + ((\lambda_i - 1)D_j[\mathbf{u}], Y_{nm})], \quad (16)$$

$$\left(\frac{\partial \mathbf{x}}{\partial t}, Y_{nm}\right) = (\mathbf{u}, Y_{nm}), \quad (17)$$

$$\left(\frac{\partial \Gamma}{\partial t}, Y_{nm}\right) = -(\nabla_\gamma \cdot \Gamma \mathbf{u}_\gamma, Y_{nm}) + \frac{1}{Pe} (\nabla_\gamma^2 \Gamma, Y_{nm}) - (2K \Gamma \mathbf{u} \cdot \mathbf{n}, Y_{nm}). \quad (18)$$

This approach exploits the orthogonality and symmetry properties of the spherical harmonics as discussed in [7] and it results to be cheaper compared to a standard approach where the physical variables are directly discretized, as observed already in [41]. Indeed, if the original system with physical variables has size $2(p+1)^2$ (the grid points), the Galerkin formulation almost halves the number of unknowns (the spherical coefficients). The spectral coefficients are complex (doubling the size of system), but thanks to the skew-symmetric property of real-valued functions,

$$f_n^m = (-1)^m \overline{f_n^{-m}}$$

and the fact that all coefficients with $|m| > n$ are zero, the final system has $(p+1)(p+2)$ unknowns.

1.3. Upsampling and de-aliasing

Spherical harmonics can be seen as the surface counterpart to a Fourier series for a closed curve, and in a similar way as aliasing affects discrete Fourier series, samples of distinct functions may be indistinguishable on a discrete grid when dealing with spherical harmonics. High-frequency basis functions may alias to lower frequencies on a finite p -grid and introduce pollution to lower frequencies which renders the simulation unstable. This is a typical problem when dealing with non-linear manipulation of functions (mean and Gaussian curvatures, surface gradients, etc.) and it is necessary to keep the aliasing errors under control for these calculations.

When computing geometrical quantities involving non-linear manipulations, we will therefore first upsample the surface and the functions involved to a finer grid,¹ perform differentiation and non-linear manipulations, and then downsample¹ the result to the original grid. The commonly used “3/2 upsampling rate” [36] is not a good choice for our purposes since highly non-linear functions are involved for which this standard upsampling rate might not be sufficient. The adequate upsampling rate depends on the specific shape of the surface, and we will adopt an adaptive upsampling procedure introduced by Rahimian et al. [41] which is based on the decay of the mean curvature spectrum.

¹ By upsampling we mean to pad with zeros in the spectral space and then transform back to a finer grid in physical space. By downsampling back again we mean to transform to spectral space, cut the extra modes and transform back to the original grid in physical space.

2. Numerical integration

2.1. Regular integrals and discrete orthogonality

We will use a Gaussian spherical grid: in the longitudinal direction we discretize $\phi \in [0, 2\pi)$ using $2p + 2$ equidistant points $\{\phi_i = \frac{\pi i}{p+1}\}_{i=0}^{2p+1}$, while in the non-periodic direction $\theta \in [0, \pi]$ we set $\{\theta_j = \cos^{-1}(t_j)\}_{j=0}^p$, where $t_j \in [-1, 1]$ are the Gauss–Legendre quadrature nodes with corresponding Gaussian quadrature weights w_j^G . This is a standard choice for spectrally accurate integration when using a spherical harmonics expansions [41,53,51].

Now we can define a quadrature rule for regular integrals:

$$\int_{\gamma} f d\gamma = \sum_{j=0}^p \sum_{k=0}^{2p+1} w_j f(\theta_j, \phi_k) W(\theta_j, \phi_k), \quad (19)$$

where $w_j = \frac{\pi}{p} \frac{w_j^G}{\sin(\theta_j)}$ and $W(\theta_j, \phi_k)$ is the infinitesimal area element of the surface γ .

This choice of quadrature rule ensures the discrete orthogonality property:

$$(Y_n^m, Y_{n'}^{m'})^p = \delta_{nn'} \delta_{mm'}, \quad (20)$$

for $0 \leq n, n' \leq p$ and $|m| \leq n, |m'| \leq n'$, see [10] for details.

In this setting, the discrete version of eq. (12) is:

$$f_n^m = \int_0^\pi \int_0^{2\pi} f(\theta, \phi) \overline{Y_n^m(\theta, \phi)} \sin \theta d\theta d\phi \approx \frac{\pi}{p} \sum_{i=1}^{(p+1)2} \sum_{j=1}^{(p+1)2} w_j^G f(\theta_i, \phi_j) \overline{Y_n^m(\theta_i, \phi_j)}. \quad (21)$$

We will refer to eq. (21) as regular quadrature. Fast algorithms for computing backward and forward spherical harmonics transforms based on this grid are available [34], [42].

2.2. Singular integration

When computing the integrals in (4), for $\mathbf{x}_0 = \mathbf{x}$ we have a singularity. In order to compute the integrals we will make use of the following theorem [19,22]:

Theorem 1. For any smooth function f defined on a C^∞ surface γ globally parametrized by spherical coordinates (θ, ϕ) , the harmonic potential evaluated at the north pole $\mathbf{x}(0, 0)$ is given by

$$I[f](0, 0) = \int_0^\pi \int_0^{2\pi} \frac{f(\mathbf{x}(\theta, \phi)) W(\theta, \phi)}{|\mathbf{x}(0, 0) - \mathbf{x}(\theta, \phi)|} d\theta d\phi,$$

where W represents the infinitesimal area element. For the quadrature rule

$$Q[f](0, 0) = \sum_{j=0}^p \sum_{k=0}^{2p+1} \frac{w_j^S}{|\mathbf{x}(0, 0) - \mathbf{x}(\theta_j, \phi_k)|} f(\mathbf{x}(\theta_j, \phi_k)) \frac{W(\theta_j, \phi_k)}{\sin(\theta_j)} \quad (22)$$

where

$$w_j^S = w_j \sum_{n=0}^p 2 \sin(\theta_j/2) P_n(\cos \theta_j), \quad (23)$$

it holds that Q converges superalgebraically to I with p .

The theorem is based on the fact that the spherical harmonics are eigenfunctions of the Laplace operator on the sphere. It can be extended to the single and double layer kernels of Stokes flow using symmetries and smoothness properties as shown in [53,41]. Using the quadrature rule (22) we can hence achieve an exponential convergence for the integrals that need to be computed in (4).

The theorem is stated for the target point \mathbf{x}_0 at the north pole of the parametrization, and does not hold in general. Hence, for any target point on the surface, the coordinate system will be rotated such that this quadrature rule can be applied. Analytical expressions for rotating the coefficients of the spherical harmonic expansion are given in Appendix B. A fast algorithm for spherical grid rotation with application to singular quadrature is given by Gimbutas and Veerapaneni [21] where the computational complexity for all targets on the surface is $O(p^4 \log p)$.

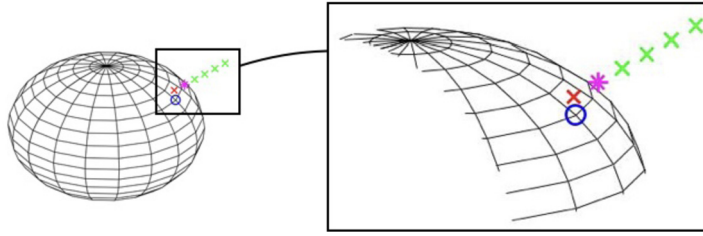


Fig. 1. Schematic picture of the special quadrature for the nearly singular integrals. The pink star represents the target point \mathbf{x}_0 , the blue circle is the closest grid point used as starting point for the Newton iteration (26). The red cross represents \mathbf{x}_* , the projection on the surface of the target point \mathbf{x}_0 , and the green crosses are the points far away from the surface used for the 1D interpolation.

2.3. Nearly-singular integration

As two drops get closer, the integrals in Eq. (4) get more difficult to evaluate accurately due to the near singularities in the integrals, see Fig. 2(a). For this situation we have no analytical treatment as in the singular case. The nearly singular integration in 3D remains an area of active research, both for fixed and time-dependent geometries. In the first case, data can be precomputed and stored in order to accelerate the algorithm, but this is not possible in our case when the geometry is moving and deforming. Most of the methods available are based on refinement and/or interpolation techniques: Zhao et al. [61] proposed a technique based on the method of floating partition of unity for both singular and nearly singular integrals; Bremer and Gimbutas [11,12] describe a modified Nyström method for the discretization of weakly singular integral operators by first applying a suitable transformation to simplify the integrand and then using a precomputed table of quadrature rules to evaluate the resulting integral efficiently; Tlupova and Beale [51] developed a third order method using a regularized kernel, and, more recently, af Klinteberg and Tornberg [3] presented a fast and accurate method based on QBX (quadrature-by-expansion) for spheroidal surfaces, utilizing precomputation for efficiency. Ying, Biros and Zorin [58] proposed a procedure based on interpolation to compute the nearly-singular integrals. We will adapt and refine the last approach for our application.

When the drops are well separated, at some distance larger than $\tilde{A}(h)$ from each other (where h is a characteristic grid spacing), the regular quadrature works well. As they get closer, regular quadrature on a finer grid can still be used. Here, the density is interpolated to the finer (upsampled) grid, where the nearly singular kernel is better resolved. But at some point, a special quadrature method is needed since the quadrature error grows exponentially as we approach the surface [3] and it is not possible to resolve the problem by grid refinement, i.e. upsampling.

To formalize this division into regions, let \mathbf{x}_0 denote the target point and $h = \frac{R\pi}{p+1}$ the grid size, where R is the mean radius of the drop. We consider the following three regions:

- Well separated: $\Omega_0 = \{\mathbf{x}_0 \in \gamma_i \mid \text{dist}(\mathbf{x}_0, \gamma^* \setminus \gamma_i) \in (\tilde{A}(h), \infty), i = 1, \dots, N\}$:
A regular quadrature rule on the standard grid is used;
- Intermediate: $\Omega_1 = \{\mathbf{x}_0 \in \gamma_i \mid \text{dist}(\mathbf{x}_0, \gamma^* \setminus \gamma_i) \in (h, \tilde{A}(h)], i = 1, \dots, N\}$:
A regular quadrature rule on the grid upsampled by a factor \tilde{U} is used;
- Nearest: $\Omega_2 = \{\mathbf{x}_0 \in \gamma_i \mid \text{dist}(\mathbf{x}_0, \gamma^* \setminus \gamma_i) \in (0, h], i = 1, \dots, N\}$:
In this case using the upsampled grid is not enough and we need a special technique to compute the nearly-singular integral, as will be described below.

The idea introduced in Ying et al. [58] for the nearly singular integration was to find the point \mathbf{x}_* on the surface that is closest to the target point \mathbf{x}_0 . Then, continuing along a line that passes through \mathbf{x}_* and \mathbf{x}_0 , the integral is evaluated at a number of points $\mathbf{x}_1, \dots, \mathbf{x}_n$ further away from the surface (see Fig. 1). This can be done by regular quadrature on the standard grid or on the upsampled grid, depending on if the point belongs to Ω_0 or Ω_1 . The value of the integral on the surface (at \mathbf{x}_*) needs to be computed by the special quadrature for singular integrals discussed in section 2.2. At this point a 1D Lagrangian interpolation is used to compute the value at \mathbf{x}_0 by interpolating the values at \mathbf{x}_* and $\mathbf{x}_i, i = 1, \dots, N$.

We will follow the same approach as above in the following way. A cell list algorithm has been implemented to find in which region the target point \mathbf{x}_0 belongs. For the regions Ω_0 and Ω_1 , the regular quadrature rule has already been introduced in Section 2.1. For the target points belonging to the region Ω_2 , we need to find the closest point on the surface, \mathbf{x}_* . Using the cell list mentioned above, we can also find the closest grid point to \mathbf{x}_0 (see Fig. 1); then we use it as starting point for a Newton iteration to find the closest point on the surface (not necessarily a grid point). We need to minimize the distance between the closest drop surface and the target point. Since the surface is represented by a spherical harmonic expansion, we want to find the parameters (ϕ, θ) corresponding to the point which minimizes the distance

$$\min_{(\phi, \theta)} \|\mathbf{x}(\phi, \theta) - \mathbf{x}_0\| = \min_{(\phi, \theta)} \left\| \sum_{n=0}^p \sum_{m=-n}^n \mathbf{x}_n^m Y_n^m(\phi, \theta) - \mathbf{x}_0 \right\|$$

(where \mathbf{x}_n^m are the spherical harmonic coefficients of the drop surface, eq. (14).)

To solve this optimization problem, we look for the zeros of the gradient of

$$f(\phi, \theta) = \|\mathbf{x}(\phi, \theta) - \mathbf{x}_0\|^2,$$

where we have

$$\frac{\partial f}{\partial \phi} = 2 \left(\sum_n \sum_m \mathbf{x}_n^m Y_n^m - \mathbf{x}_0 \right) \cdot \left(\sum_n \sum_m \mathbf{x}_n^m \frac{\partial Y_n^m}{\partial \phi} \right) = 0 \quad (24)$$

$$\frac{\partial f}{\partial \theta} = 2 \left(\sum_n \sum_m \mathbf{x}_n^m Y_n^m - \mathbf{x}_0 \right) \cdot \left(\sum_n \sum_m \mathbf{x}_n^m \frac{\partial Y_n^m}{\partial \theta} \right) = 0 \quad (25)$$

We solve the system (24)–(25) using a Newton iterative method,

$$(\phi^{n+1}, \theta^{n+1}) = (\phi^n, \theta^n) - H^{-1} \nabla(f(\phi^n, \theta^n)) \quad (26)$$

where H is the Hessian of f .²

Once \mathbf{x}_* has been determined, we could apply Theorem 1 for computing the integral at this location. We have however already computed the single and double layer integrals for the *self-self* interaction with all grid points on the surface as target points, and these discrete values in term determine a spherical harmonics expansion of the field over the surface. Hence, we can simply use this expansion to determine the value at \mathbf{x}_* , and this same expansion can be used for any target point close to the surface where the special quadrature is invoked. This approach is computationally cheaper than the direct application of Theorem 1 even if it is used only for a single point. Finally, the interpolation procedure previously described to obtain the potential at the target point \mathbf{x}_0 can be used.

In this procedure, there are a number of parameters to set,

- \tilde{A} , the maximum distance before we need to upsample the grid for the regular quadrature,
- \tilde{U} , the upsampling rate used in the intermediate region,
- L , the number of points used for interpolation for target points in the nearest region,
- \tilde{D} , the distance between these points.

Clearly all these parameters depend on the resolution, so we will express them in terms of h , and we will see in the next section how they affect the accuracy. There are two sources of errors that contribute to the quadrature error in the nearest region. Firstly, errors in evaluating the values along the 1D line that will be used for interpolation. These errors arise from applying the singular, upsampled or regular quadrature rule to targets respectively on the surface, in the intermediate or in the well-separated region, depending on where the points fall. The interpolation procedure then introduces an additional error. An error bound is given for the special quadrature rule in [58]: assuming the boundary surface to be infinitely smooth, it provides a convergence rate that depends on the regularity of the density or if that is high enough (if the density is smooth, the convergence is spectral), the order of polynomial interpolation. We are using a different basic quadrature rule as compared to [58], but with similar convergence properties. These error bounds however include unknown constants, and can not be used to determine the level of the error for a given grid size. Hence, it is not possible to take advantage of the error bounds in practice, when setting the special quadrature parameters.

2.3.1. Testing the nearly singular quadrature

We will first test the nearly-singular quadrature algorithm for the double-layer potential on a unit sphere; in Fig. 2 it is shown how the error behaves with and without special quadrature. We notice that the upsampled region is not big enough if we fix the distance $\tilde{A} = \sqrt{h}$ as suggested in [58] (Fig. 2(b)), but $5h$ seems to be safer to ensure good accuracy (Fig. 2(c)). For this specific case the error is computed for the double-layer identity, where we know the analytical solution:

$$\int_{\Gamma} T_{ijk}(x, y) \hat{n}_k(y) ds(y) = \delta_{ij} \begin{cases} 0 & \text{if } x \text{ outside } \Gamma, \\ 4\pi & \text{if } x \in \Gamma, \\ 8\pi & \text{if } x \text{ inside } \Gamma. \end{cases}$$

² Note that the inverse of H might be not well defined. To avoid this problem, an approach exploited in the Levenberg–Marquardt algorithm (which uses an approximate Hessian) is to add a scaled identity matrix to the Hessian, μI . This results in slower but more reliable convergence where the Hessian does not provide useful information [16].

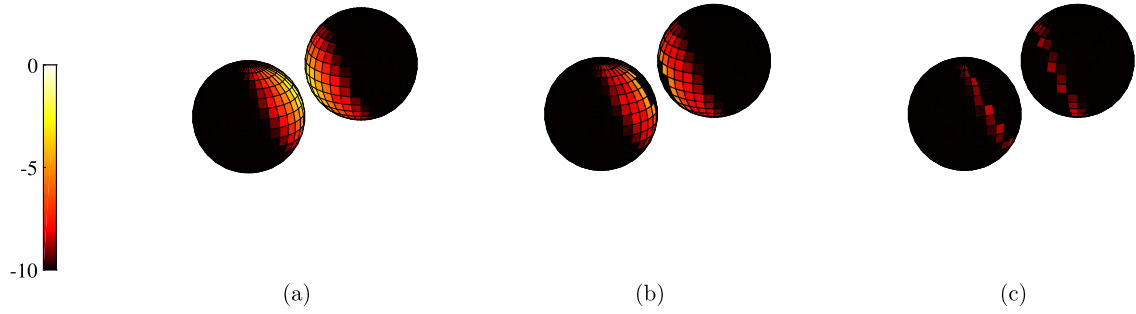


Fig. 2. Error (log scale) in computing the double-layer identity, $p = 15$. (a) Regular quadrature; (b) Special quadrature with $\tilde{A} = \sqrt{h}$, $\tilde{U} = 4$; (c) Special quadrature with $\tilde{A} = 5h$, $\tilde{U} = 4$.

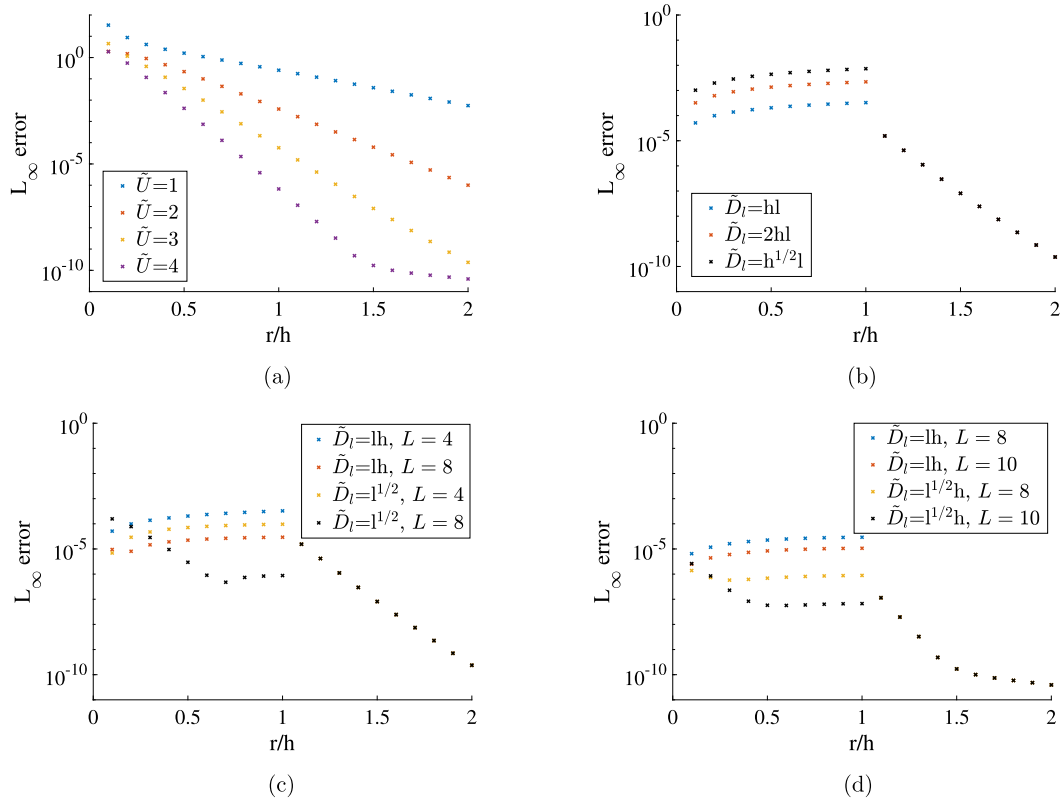


Fig. 3. L_∞ norm of the error for the analytical test given by [15–26] vs the relative distance r/h ; r is the distance between the target point and the ellipsoid and $h = \frac{\pi}{p+1}$, $p = 39$. (a) Regular quadrature with different upsampling rates; (b) Special quadrature with $L = 4$ uniformly distributed interpolating points in the *Nearest region* and regular quadrature on the upsampled grid with $\tilde{U} = 3$ in the *Intermediate region*; (c) Special quadrature with $L = 4, 8$ uniformly and non-uniformly distributed interpolating points in the *Nearest region* and regular quadrature on the upsampled grid with $\tilde{U} = 3$ in the *Intermediate region*; (d) Special quadrature with $L = 8, 10$ uniformly and non-uniformly distributed interpolating points in the *Nearest region* and regular quadrature on the upsampled grid with $\tilde{U} = 4$ in the *Intermediate region*.

This solution is constant outside the surface, and therefore inadequate for studying the convergence of the interpolation method (sketch in Fig. 1), so we will use instead an analytical non-constant solution given by Jeffery [26,15] for a spheroid with aspect ratio (1:2) to analyze the method. In Fig. 3 we compare the error obtained by regular quadrature with the one obtained by the special quadrature for different choices of the parameters \tilde{U} , \tilde{D}_l and L . In Fig. 3(b) we test uniformly distributed points for the interpolation, where the distance between points is constant and depends only on the resolution parameter h ; in this sense the distribution of points is linear in l . We tried different choices: $\tilde{D}_l = hl$, $\tilde{D}_l = 2hl$, $\tilde{D}_l = \sqrt{hl}$, $l = 1, \dots, L$, but in none of these cases the accuracy is sufficient, indeed we observe a jump between the regular quadrature with upsampling and the special quadrature. We observe that using a higher upsampling rate \tilde{U} always gives lower errors. Also when we consider a sequence of interpolation points that scales with the distance as $\tilde{D}_l(h) = h\sqrt{l}$ and increase the number of interpolation points, $L = 8, 10$, we can achieve higher accuracy. We can conclude that using the spacing given by

$\tilde{D}_I(h) = h\sqrt{l}$ together with a sufficiently large \tilde{U} and L we can reach the desired tolerance; of course these parameters need to be increased and tuned carefully to avoid unnecessary computational costs.

3. Time-stepping

The choice of the time-stepping scheme for updating the drop positions and the surfactant evolution has to consider two main aspects: the computational cost and the control of error. The main numerical cost comes from solving the integral equation to obtain the velocity of the drops as presented in the previous sections. We want to maintain the number of Stokes evaluations at a minimum; at the same time the numerical scheme for the time evolution needs to control the error in both quantities (drop shape/surfactant concentration) and the time-step size should be adaptive balancing these two factors.

We recall that the system of ODEs (drop/surfactant) we are considering is given by

$$\begin{cases} \frac{d\mathbf{x}}{dt} = \mathbf{u}(\mathbf{x}, \sigma), \\ \frac{d\Gamma}{dt} = f_E(\mathbf{x}, \mathbf{u}, \Gamma) + f_I(\mathbf{x}, \Gamma), \end{cases} \quad (27)$$

where the velocity \mathbf{u} at the interface is given by the solution of the boundary integral equations (4), f_E and f_I represents respectively the convective and the diffusion component of the equation for the surfactant (see eq. (5)),

$$\begin{aligned} f_E &= -\nabla_\gamma \cdot (\Gamma \mathbf{u}_\gamma) - 2K(\mathbf{x})\Gamma(\mathbf{u} \cdot \mathbf{n}), \\ f_I &= \frac{1}{Pe} \nabla_\gamma^2 \Gamma. \end{aligned}$$

Due to the different nature of these two terms, we would like to treat them differently: an implicit scheme is a good choice for the diffusion term and an explicit method for the convective term [6].

We will first introduce three explicit schemes for the drop evolution (Section 3.1), then an IMEX scheme for the surfactant concentration (Section 3.2), with particular attention to the treatment of the implicit term; the coupling drop/surfactant is briefly explained in Section 3.3 where we also compare the different schemes considered.

3.1. Drop evolution

For the drop evolution we compare three different adaptive Runge–Kutta schemes, with corresponding Butcher tableaux given by:

Explicit midpoint
(2nd order)

$$\begin{array}{c|c} 0 & \\ \hline 1/2 & 1/2 \\ \hline & 0 \quad 1 \\ & 1 \quad 0 \end{array}$$

RK23
(Bogacki–Shampine, 3rd order)

$$\begin{array}{c|ccc} 0 & & & \\ \hline 1/2 & 1/2 & & \\ 3/4 & 0 & 3/4 & \\ \hline 1 & 2/9 & 1/3 & 4/9 \\ & 2/9 & 1/3 & 4/9 \\ & 7/24 & 1/4 & 1/3 \quad 1/8 \end{array}$$

Kutta's method
(3rd order)

$$\begin{array}{c|ccc} 0 & & & \\ \hline 1/2 & 1/2 & & \\ 1 & -1 & 2 & \\ \hline & 1/6 & 4/6 & 1/6 \\ & 0 & 1 & \end{array}$$

The bottom line represents the lower order scheme; the difference between the two approximate solutions at time $t + dt$ produced by the two methods provides an estimate of the local truncation error for the scheme of lower order, then the solution given by the highest method is employed so that the resulting scheme will have the highest order [40].

3.2. Surfactant evolution

For the surfactant evolution we consider a 2nd order IMEX Runge–Kutta Scheme [6] with time step size dt as follows:

- $\tilde{k}_0 = f_E(\mathbf{x}^{(t)}, \mathbf{u}^{(t)}, \Gamma^{(t)});$
- solve for $\Gamma^{(t+dt/2)}$ (see Section 3.2.1 for more details):

$$\Gamma^{(t+dt/2)} = \Gamma^{(t)} + dt/2 [f_E(\mathbf{x}^{(t)}, \mathbf{u}^{(t)}, \Gamma^{(t)}) + \frac{1}{Pe} \nabla_\gamma^2 \Gamma^{(t+dt/2)}], \quad (28)$$

and compute

$$k_{1/2} = f_I(\mathbf{x}^{(t+dt/2)}, \Gamma^{(t+dt/2)});$$

$$\bullet \tilde{k}_{1/2} = f_E(\mathbf{x}^{(t+dt/2)}, \mathbf{u}^{(t+dt/2)}, \Gamma^{(t+dt/2)});$$

$$\Gamma^{(t+dt)} = \Gamma^{(t)} + dt(\tilde{k}_{1/2} + k_{1/2}). \quad (29)$$

The input data $\mathbf{u}^{(i)}$, for $i = t, t + dt/2$, and the corresponding position vectors $\mathbf{x}^{(i)}$, are given by the time-solver for the drop evolution (see Algorithm 1).

Since we want an adaptive method able to keep the error below a fixed tolerance, we compare two methods to control the surfactant evolution:

1. Error computed with IMEX1 (1st order):

$$\Gamma_{IMEX1}^{(t+dt)} = \Gamma^{(t)} + dt(f_E(\mathbf{x}^{(t)}, \mathbf{u}^t, \Gamma^{(t)}) + f_I(\mathbf{x}^{(t+1)}, \Gamma_{IMEX1}^{(t+dt)})); \quad (30)$$

in this case the estimation of the error is given by

$$err_{surfactant}^{(t+dt)} = \frac{\|\Gamma^{(t+dt)} - \Gamma_{IMEX1}^{(t+dt)}\|_\infty}{\|\Gamma^{(t+dt)}\|_\infty} \quad (31)$$

and then it requires two numerical solutions to be computed.

2. Error based on the local conservation of surfactant (*conservation error*): in the case of insoluble surfactant the mass is conserved on the interface,

$$\frac{d}{dt} \int_{\gamma(t)} \Gamma dS = 0.$$

As an estimate for the surfactant error, we compute the local error in conservation of mass

$$err_{surfactant}^{(t+dt)} = \frac{|\int_{\gamma(t+dt)} \Gamma^{(t+dt)} dS - \int_{\gamma(t)} \Gamma^{(t)} dS|}{|\int_{\gamma(t)} \Gamma^{(t)} dS|}, \quad (32)$$

where by *local* we refer to the change in mass between the current and the previous time-step and where the integral is evaluated numerically as explained in Section 2.1. This choice does not compute the error of $\Gamma^{(t+dt)}$ directly but through a physical quantity of interest as in (31); at the same time it is computationally cheaper than the previous option since only one numerical solution is needed to compute (32).

We also considered a Semi-implicit Spectral Deferred Correction Method [33,39] but it turned out to be too expensive for our problem since it requires several BIM solver calls to achieve the desired tolerance for the coupled system.

3.2.1. Preconditioning

Using the IMEX scheme for the surfactant, we need to solve the system generated by eq. (28) for every time step at the stage $(t + dt/2)$, which we can write in a compact form as:

$$\mathbf{A}\mathbf{y} = \mathbf{b} \quad (33)$$

where

$$\mathbf{A} = \mathbf{I} - \frac{dt}{2} \frac{1}{Pe} \nabla_S^2,$$

$$\mathbf{b} = \Gamma^{(t)} + \frac{dt}{2} f_E(\mathbf{x}^{(t)}, \mathbf{u}^{(t)}, \Gamma^{(t)}),$$

and $\mathbf{y} = \Gamma^{(t+dt/2)}$. In practice we actually solve the system for the spherical harmonics coefficients, see eq. (18).

The conditioning of this system gets worse with increased diffusion, so we need a preconditioner to accelerate the convergence. It is well known that the spherical harmonics are eigenfunctions of the Laplace–Beltrami operator on the sphere [7],

$$\Delta_{\mathbb{S}^2} Y_n^m = -n(n+1) Y_n^m. \quad (34)$$

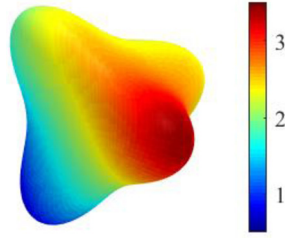


Fig. 4. Surface used to test the preconditioner; the colors denote the surfactant concentration.

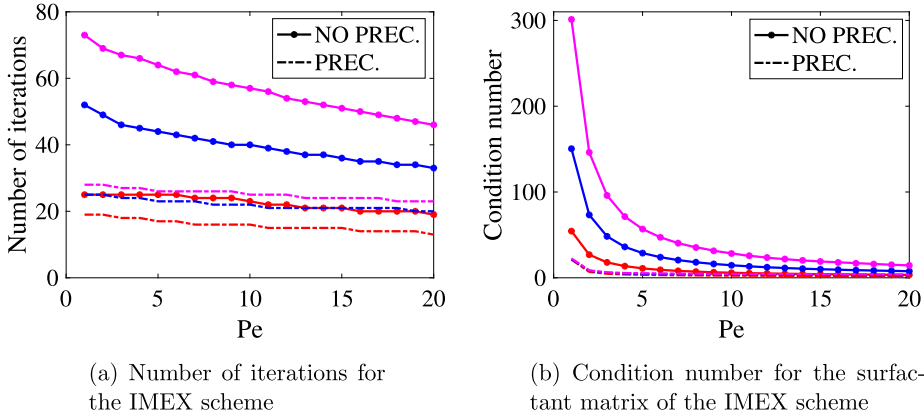


Fig. 5. The effect of the preconditioner for the IMEX scheme for different resolutions: $p = 9, 15, 21$ respectively represented by the red, blue and magenta colors. When applying the preconditioner introduced in Section 3.2.1 the number of iterations needed is strongly reduced as well as the condition number, which becomes of the same order independent of p .

We use the diagonal matrix resulting on a sphere as a preconditioner for a general problem (general surface). In the following plots we are comparing the number of iterations (GMRES $\text{tol}=10e-12$) for different diffusion coefficients (different Pe) with initial concentration $\Gamma = 2 + \mathbf{x}$, on the surface³ showed in Fig. 4.

In Fig. 5(a) we show a substantial reduction in the number of iterations needed for the preconditioned algorithm and a gain increasing with the order of spherical harmonics; we also show (Fig. 5(b)) the condition number of the matrix A compared to the condition number of the preconditioned matrix $B = S^{-1}A$, where S is the diagonal matrix obtained on the sphere, and we observe that, when the preconditioner is used, the condition number remains of the same order for all the different orders of spherical harmonics expansion considered.

3.3. Coupling and comparison

The explicit scheme for the drop evolution and the IMEX scheme for the surfactant concentration evolution need to be coupled together, as shown in the pseudo-code Algorithm 1 for the specific coupling Midpoint/IMEX. We would like the drop surface and the surfactant concentration evolutions to use the same temporal stages, and this is the basic reason why we considered and restricted the comparison to the above mentioned schemes. Indeed, they all use the same stages with an exception given by the case of RK23 where we would need an extra computation of the surfactant at $t + \frac{3}{4}dt$. This can be done in two ways: either we half the time-step for the surfactant (but we would do an extra unnecessary computation in $t + dt/4$), or we simply compute the solution in $t + \frac{3}{4}dt$ using a first order IMEX method with time-step $dt/4$, i.e. we solve for $\Gamma^{t+\frac{3}{4}dt}$:

$$\Gamma^{(t+\frac{3}{4}dt)} = \Gamma^{(t+dt/2)} + \frac{dt}{4}(f_E(\mathbf{x}^{(t+dt/2)}, \mathbf{u}^{(t+dt/2)}, \Gamma^{(t+dt/2)}) + f_I(\mathbf{x}^{(t+\frac{3}{4}dt)}, \Gamma^{(t+\frac{3}{4}dt)})).$$

³ The surface is given by:

$$\begin{cases} x_1(\theta, \phi) = \rho(\theta, \phi)\cos(\phi)\sin(\theta); \\ x_2(\theta, \phi) = \rho(\theta, \phi)\sin(\theta)\sin(\phi); \\ x_3(\theta, \phi) = \rho(\theta, \phi)\cos(\theta) \end{cases}$$

with $\rho(\theta, \phi) = 0.7 + 0.3e^{-3Re(Y_3^2(\theta, \phi))}$.

We adopt the second choice. The value produced is never used for the surfactant itself but only to update an intermediate stage of the drop evolution; indeed, it does not seem to affect the overall accuracy as observed by numerical tests.

From numerical tests we observed that both the third order schemes RK23 and Kutta's method behave like a second order scheme as well as the Midpoint scheme (as expected); this is not surprising since the drop evolution is coupled together with the second order IMEX scheme for the surfactant. Once we introduce adaptivity in the time-step selection based on both surfactant and drop evolution, we can observe that the *conservation error* is a good choice for adaptivity only when using the Midpoint scheme, whilst for the other two schemes the error is not below the prescribed tolerance (Fig. 7). In the same figure we can see that when IMEX1 is used for the adaptivity in the surfactant, the error is lower, even too low for the drop evolution (Fig. 7(a)) when using RK23 or Kutta's method; in these two cases, the number of Stokes evaluations (which represents the main cost) is the same for the two schemes, and lower for the Midpoint scheme (Fig. 6(a)). The Midpoint scheme is the only one which respects the prescribed tolerance in the drop and in the surfactant using both IMEX1 and the conservation error. Since the adaptivity with the conservation error needs only one numerical solution despite the two needed for the adaptivity given by IMEX1, the Midpoint rule is the natural choice. Note that for these simulations we used a rather large expansion order p in order to make sure that the relative error is independent from the spatial resolution; the error flattens out when the tolerance decrease (Fig. 7) due to the fixed imposed maximum step-size.

Concluding, we find that the best combinations of methods for the evolution of the coupled system drop/surfactant is the Midpoint rule (drop) together with the second order IMEX scheme that uses the conservation error for adaptivity.

Algorithm 1 Coupling the drop/surfactant evolution in time (Midpoint+IMEX).

```

while  $t < T_{max}$  do
  • Given  $\mathbf{x}^{(t)}$ ,  $\Gamma^{(t)}$ , compute velocity  $\mathbf{u}^{(t)}$  by solving eq. (16).

      ↓↓

  •  $\mathbf{x}^{(t+dt/2)} = \mathbf{x}^{(t)} + \frac{dt}{2} \mathbf{u}^{(t)}$ ;
  • Compute  $\Gamma^{(t+dt/2)}$  by solving the system in (28);
  • Given  $\mathbf{x}^{(t+dt/2)}$ ,  $\Gamma^{(t+dt/2)}$ , compute velocity  $\mathbf{u}^{(t+dt/2)}$  by solving eq. (16).

      ↓↓

  •  $\mathbf{x}^{(t+dt)} = \mathbf{x}^{(t)} + dt \mathbf{u}^{(t+dt/2)}$ ;
  • Compute  $\Gamma^{(t+dt)}$  using eq. (29).

```

Adaptivity in time^a

$err = \max(err_{drop}, err_{surfactant});$

if $err < tol$ **then**

Reparametrization \rightarrow Algorithm 2;

$t = t + dt;$

end if

$dt = dt(0.9 \frac{tol}{err})^{1/2}$

end while

^a The formula given for updating the time-step is for a second order method and the power 1/2 depends on this order; 0.9 is a safety factor to ensure the new dt sufficiently small [23].

4. Reparametrization

The spherical harmonics representation can be seen as a mapping from a Gaussian grid to the 3D surface. This mapping is not unique for a given surface (see Fig. 8) and the optimal map⁴ is not known a priori for a general surface. When performing numerical simulations, significant distortions of the point distributions on the drop surfaces may arise, especially for long simulations. This can introduce unresolvable high-frequency components (Fig. 8(b)), aliasing errors and numerical

⁴ Optimal in the sense of modes needed. For the easiest example of the sphere we know that the optimal choice is the one that needs only one mode, see Fig. 8(a).

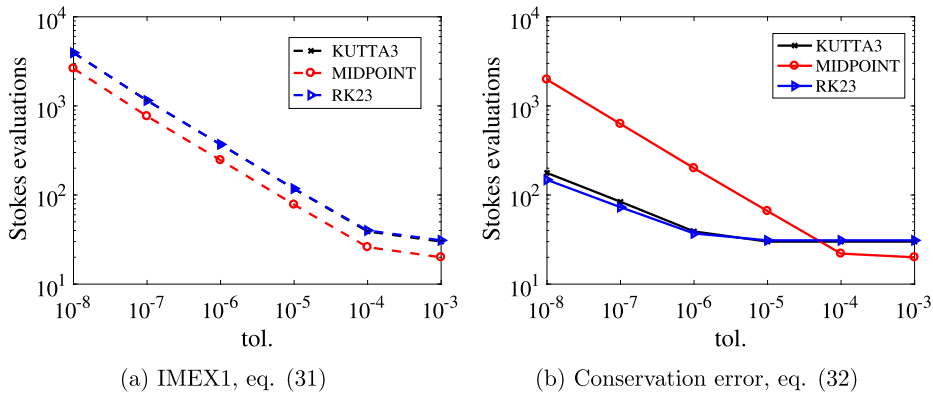


Fig. 6. The number of Stokes evaluations plotted versus tolerance using the two different estimates for the surfactant error. For this simulation we used: $p = 21$, final time $T = 1$, initial shape: ellipsoid ($a/c = 1/2$) with initial surfactant concentration $\Gamma = 1 + x$ immersed in a shear flow with $Ca = 0.2$, $\lambda = 1$, $Pe = 10$, $E = 0.2$, $x_s = 0.3$.

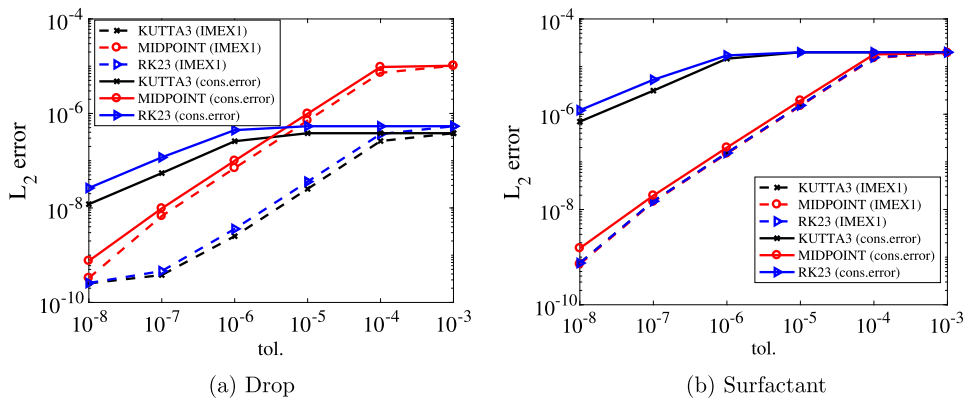


Fig. 7. Relative error vs tolerance. We compare the error (L2-norm) for the drop position and surfactant concentration. The data of this simulation are the same as in Fig. 6, the reference solution is computed using the Midpoint scheme combined with the second order IMEX scheme and a fixed time-step $\Delta t = 10^{-5}$.

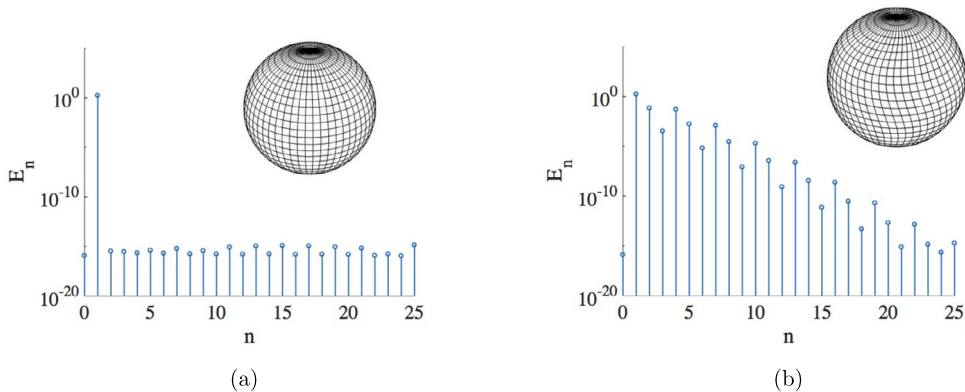


Fig. 8. (a) Standard and (b) distorted grids on a unit sphere with related spectra $E_n(\mathbf{x}) := (\sum_{m=-n}^n |\mathbf{x}_n^m|^2)^{1/2}$ plotted versus n .

instability. For this reason we need to introduce a reparametrization algorithm which seeks to minimize a spectral energy, optimizing the grid point distribution with respect to the spherical harmonic representation. We will begin by describing the approach used in [53,41]. Here, the authors introduce a smooth function $F : \mathbb{R}^3 \rightarrow \mathbb{R}$, which is the implicit representation of a general surface γ , and a quality measure $E(\mathbf{x}) : X \rightarrow \mathbb{R}$, where X is a space of sufficiently smooth functions on \mathbb{S}^2 . It is shown how the solution of the optimization problem

$$\min_{\mathbf{x} \in X} \{E(\mathbf{x}(\theta, \phi))\}, \text{ subject to } F(\mathbf{x}(\theta, \phi)) = 0, \quad (35)$$

is given by

$$\mathbf{g} := (I - \mathbf{n}(\mathbf{x}) \otimes \mathbf{n}(\mathbf{x})) \nabla E(\mathbf{x}) = 0, \quad F(\mathbf{x}) = 0. \quad (36)$$

The authors [53] suggest to use the quality measure (or energy)

$$E(\mathbf{x}) = \sum_{n=0}^p \sum_{m=-n}^n a_{nm} |\mathbf{x}_n^m|^2, \quad (37)$$

where a_{nm} is some attenuation coefficient and \mathbf{x}_n^m are the coefficients of the spherical harmonic expansion of the position vector \mathbf{x} .

Eq. (36) can be solved by introducing a fictitious time (or pseudo-time) τ and looking for stationary solution of

$$\begin{cases} \frac{\partial \mathbf{x}}{\partial \tau} + (I - \mathbf{n}(\mathbf{x}) \otimes \mathbf{n}(\mathbf{x})) \nabla E(\mathbf{x}) = 0, \\ \mathbf{x}(0) = \mathbf{x}_0. \end{cases} \quad (38)$$

A maximum number of iterations i_{max} and a tolerance ϵ are set for the breaking criteria, where ϵ is a parameter to control the change in the distribution of points (see the original references for more details). Note that the condition $F(\mathbf{x}) = 0$ is embedded in the continuous formulation. In [53,41], eq. (38) is discretized using the forward Euler scheme and the discrete surface points are marched in pseudo time. Here, the points are not constrained to stay on the surface, which introduces an error that depends on the pseudo time step size.

The aim of the reparametrization is to penalize the high frequency components, i.e. the attenuation coefficients a_{nm} should be small for low frequencies and large for the highest ones. We can use a *Perfect Low-Pass Filter*, where $a_{nm} = 0$ if $n < n_{cutoff}$ and $a_{nm} = 1$ otherwise, or we can also use a smoother filter that increases with frequencies: $a_{nm} = 0$ if $n < n_{cutoff}$ and $a_{nm} = \frac{n}{p}$ otherwise. In [53,41] such reparametrization with a *Perfect Low-Pass Filter* and a fixed n_{cutoff} ($n_{cutoff} = \frac{p}{k_{cut}}$, $k_{cut} = 2, 3$) is used for the simulation of vesicles where it gives good results.

The main difference between vesicles and drops in this context, is that for the first case the local surface inextensibility avoids the same degree of distortions of the point distribution that can be seen for drops. We encounter a number of difficulties:

- (a) We note that the above mentioned reparametrization will not ensure volume conservation;
- (b) Using a fixed n_{cutoff} is not working well in our simulations, neither the Perfect Low-Pass Filter nor the smoother one;
- (c) The current procedure offers no spectrally accurate way to redefine the surfactant concentration on the reparameterized surface.

As for the first remark, it is certainly true also for vesicles that the volume conservation error will depend on the pseudo time step size, but it should be more noticeable for drops where distortions are larger and more reinitialization is needed.

In the following, we will introduce a new reparameterization method that resolves issues (a) and (c). We will however start by introducing an adaptive n_{cutoff} to overcome the problem (b), and show how this change by itself improves also the old reparameterization procedure.

The adaptive n_{cutoff} will depend on the geometry of the surface; in particular we fix the percentage P_{cutoff} of the modes that we want to penalize and then we compute n_{cutoff} as:

$$n_{cutoff} = \min_l \left\{ l \in \mathbb{N}, 1 < l \leq p : \frac{N_2(l)}{N_1} < P_{cutoff} \right\} \quad (39)$$

where $N_2(l) = \sum_{n=l}^p \sum_{m=-n}^n |\mathbf{x}_n^m|^2$ and $N_1 = N_2(1)$. This adaptive choice can much better determine what frequencies need to be cut for a given geometry. A basic example is a distorted grid on a sphere (as in Fig. 8(b)): in this case we know that only one mode is needed for the optimal distribution of points (Fig. 8(a)), and we reach this state using the adaptive n_{cutoff} but not using a fixed n_{cutoff} (in which case only modes higher than $p/2$ would be filtered out). Numerical experiments show that the new procedure works better also for more complicated problems, like drops immersed in a linear flow that reach a steady state. In this case the drop shape is steady but due to tangential velocities on the drop surface the point distribution is continuously changing and the reparametrization plays a fundamental role. To show this, we consider a clean drop immersed in a flow generated in the four-roll mill

$$\nabla u = \frac{1}{2} G \begin{bmatrix} 1 + \alpha & 1 - \alpha & 0 \\ -1 + \alpha & -1 - \alpha & 0 \\ 0 & 0 & 0 \end{bmatrix},$$

where α is a parameter which specifies the relative strength of the strain rate and vorticity in the flow. The parameters which affect the evolution of the drop are set to be $Ca = 0.0718$, $\lambda = 0.118$ and $\alpha = 0.6$. Under these conditions, the drop reaches a steady state, meaning that the energy defined in eq. (37) should reach a constant value. In Fig. 9 this expected

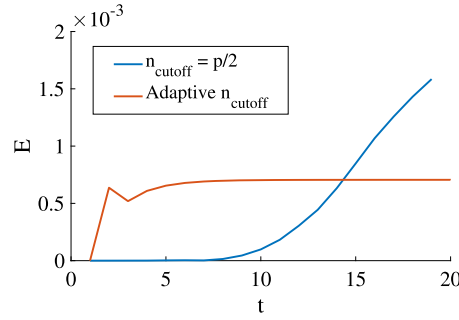


Fig. 9. Comparing the quality measure E defined in (37) using adaptive and non-adaptive n_{cutoff} . This quantity does not approach a steady state when using the fixed $n_{\text{cutoff}} = p/2$. Using the adaptive n_{cutoff} the steady state is reached in good agreement with experimental results [9].

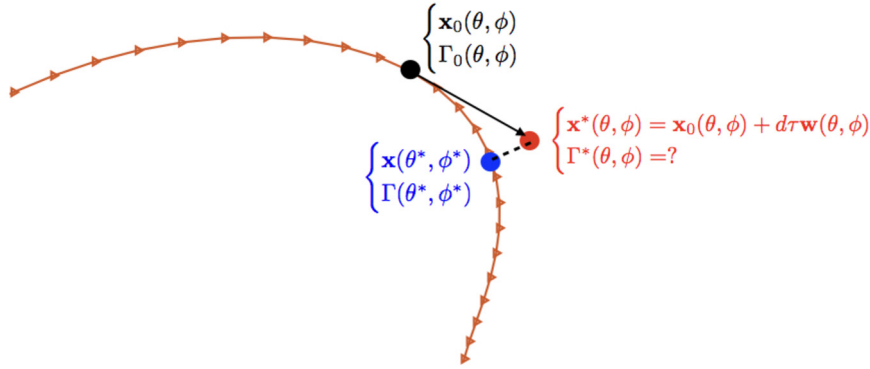


Fig. 10. Sketch of the problem for the reparametrization.

behavior can be seen using the adaptive n_{cutoff} , but for a fixed $n_{\text{cutoff}} = p/2$ the energy continues to increase and yields an unstable simulation. Defining the deformation number as:

$$D = \frac{L - B}{L + B} \quad (40)$$

where L and B are the drop length and breadth in the flow plane respectively, for the simulation with the adaptive n_{cutoff} we find a value of $D = 0.117$, in good agreement with the experimental results presented in [9]. Since this adaptive filter works well it will be used also with the new reparametrization procedure.

As mentioned in (c), we have a quantity (the surfactant concentration) that is defined on the surface. Before starting the reinitialization procedure, we have the initial expansions $\mathbf{x}_0(\theta, \phi)$ for the drop surface and $\Gamma_0(\theta, \phi)$ for the surfactant concentration. The discrete points on the surface are given by $\mathbf{x}_0(\theta, \phi)$ evaluated in the θ and ϕ values as given in (14). In the old reinitialization procedure, we move the discrete points, and for this reason we will refer to this procedure as to the *point-reparametrization*. After they have been moved, we can compute new coefficients for this discrete set of points using the discrete transform (21). We do not however know what θ and ϕ values the new point locations correspond to in the initial expansion. If we knew that, we could compute the corresponding Γ values by simply evaluating $\Gamma_0(\theta, \phi)$ at these (θ, ϕ) values. Hence, it is the aim for the new reinitialization procedure to find these values of the angles, and for this reason we will refer to the new procedure as the *angle-reparametrization*. As an additional benefit, knowing these θ and ϕ values, we can evaluate the discrete points on the surface from the initial expansion $\mathbf{x}_0(\theta, \phi)$, which yields a spectrally accurate volume conservation.

Fig. 10 shows a 2D-sketch of the problem, also indicating that the discrete points are not constrained to stay on the surface in the *point-reparametrization* procedure. For the new procedure, we instead need to find the new angle vector (θ^*, ϕ^*) in order to evaluate both the point location and the surfactant concentration on the surface. To do this we compute a parameter pseudo-velocity $(\frac{\partial \theta}{\partial \tau}, \frac{\partial \phi}{\partial \tau})$ for evolving (θ, ϕ) in pseudo-time. From eq. (38) we have $\frac{\partial \mathbf{x}}{\partial \tau} = \mathbf{w}$, where the pseudo-velocity \mathbf{w} is given by

$$\mathbf{w}(\theta, \phi) = [u_1(\theta, \phi), u_2(\theta, \phi), u_3(\theta, \phi)] = -(I - \mathbf{n}(\mathbf{x}) \otimes \mathbf{n}(\mathbf{x})) \nabla E(\mathbf{x}).$$

By the chain rule, we have

$$\frac{d\mathbf{x}}{d\tau} = \frac{\partial \mathbf{x}}{\partial \theta} \frac{\partial \theta}{\partial \tau} + \frac{\partial \mathbf{x}}{\partial \phi} \frac{\partial \phi}{\partial \tau}. \quad (41)$$

In order to find the parameter pseudo-velocity $(\frac{\partial \theta}{\partial \tau}, \frac{\partial \phi}{\partial \tau})$, we consider the two projections, where $\langle \cdot, \cdot \rangle$ denotes the scalar product:

$$\begin{cases} \langle \frac{d\mathbf{x}}{d\tau}, \frac{\partial \mathbf{x}}{\partial \theta} \rangle = \langle \frac{\partial \mathbf{x}}{\partial \theta} \frac{\partial \theta}{\partial \tau} + \frac{\partial \mathbf{x}}{\partial \phi} \frac{\partial \phi}{\partial \tau}, \frac{\partial \mathbf{x}}{\partial \theta} \rangle \\ \langle \frac{d\mathbf{x}}{d\tau}, \frac{\partial \mathbf{x}}{\partial \phi} \rangle = \langle \frac{\partial \mathbf{x}}{\partial \theta} \frac{\partial \theta}{\partial \tau} + \frac{\partial \mathbf{x}}{\partial \phi} \frac{\partial \phi}{\partial \tau}, \frac{\partial \mathbf{x}}{\partial \phi} \rangle \end{cases} \rightarrow \begin{cases} \langle \mathbf{w}, \frac{\partial \mathbf{x}}{\partial \theta} \rangle = \frac{\partial \theta}{\partial \tau} |\frac{\partial \mathbf{x}}{\partial \theta}|^2 + \frac{\partial \phi}{\partial \tau} \langle \frac{\partial \mathbf{x}}{\partial \phi}, \frac{\partial \mathbf{x}}{\partial \theta} \rangle \\ \langle \mathbf{w}, \frac{\partial \mathbf{x}}{\partial \phi} \rangle = \frac{\partial \theta}{\partial \tau} \langle \frac{\partial \mathbf{x}}{\partial \phi}, \frac{\partial \mathbf{x}}{\partial \theta} \rangle + \frac{\partial \phi}{\partial \tau} |\frac{\partial \mathbf{x}}{\partial \phi}|^2 \end{cases}$$

which can be stated in compact form as

$$A\alpha = b, \quad (42)$$

where

$$A = \begin{bmatrix} |\frac{\partial \mathbf{x}}{\partial \theta}|^2 & \langle \frac{\partial \mathbf{x}}{\partial \phi}, \frac{\partial \mathbf{x}}{\partial \theta} \rangle \\ \langle \frac{\partial \mathbf{x}}{\partial \phi}, \frac{\partial \mathbf{x}}{\partial \theta} \rangle & |\frac{\partial \mathbf{x}}{\partial \phi}|^2 \end{bmatrix}, \quad \alpha = \begin{pmatrix} \frac{\partial \theta}{\partial \tau} \\ \frac{\partial \phi}{\partial \tau} \end{pmatrix}, \quad b = \begin{pmatrix} \langle \mathbf{w}, \frac{\partial \mathbf{x}}{\partial \theta} \rangle \\ \langle \mathbf{w}, \frac{\partial \mathbf{x}}{\partial \phi} \rangle \end{pmatrix}. \quad (43)$$

We can explicitly write

$$\alpha = A^{-1}b, \quad (44)$$

where

$$A^{-1} = \frac{1}{|\frac{\partial \mathbf{x}}{\partial \theta}|^2 |\frac{\partial \mathbf{x}}{\partial \phi}|^2 - \langle \frac{\partial \mathbf{x}}{\partial \phi}, \frac{\partial \mathbf{x}}{\partial \theta} \rangle^2} \begin{bmatrix} |\frac{\partial \mathbf{x}}{\partial \phi}|^2 & -\langle \frac{\partial \mathbf{x}}{\partial \phi}, \frac{\partial \mathbf{x}}{\partial \theta} \rangle \\ -\langle \frac{\partial \mathbf{x}}{\partial \phi}, \frac{\partial \mathbf{x}}{\partial \theta} \rangle & |\frac{\partial \mathbf{x}}{\partial \theta}|^2 \end{bmatrix}.$$

The problem can be reformulated using tensor notation and differential geometry quantities⁵ to see that we are looking for the component of the vector \mathbf{w} in the non-orthogonal tangent basis. Once we solve the system for the derivatives $(\frac{\partial \theta}{\partial \tau}, \frac{\partial \phi}{\partial \tau})$, we can compute the new parameters (θ^*, ϕ^*) using a forward Euler step. At this point the new position is given by eq. (14). One extra forward and one extra backward transform are needed in order to keep the original grid, equidistant in ϕ and Gauss–Legendre points in θ :

$$\mathbf{x}(\theta^*, \phi^*) = \sum_{n=0}^p \sum_{m=-n}^n \mathbf{x}_{(0),n}^m Y_n^m(\theta^*, \phi^*) =: \tilde{\mathbf{x}}(\theta, \phi) = \sum_{n=0}^p \sum_{m=-n}^n \tilde{\mathbf{x}}_n^m Y_n^m(\theta, \phi) \quad (45)$$

$$\Gamma(\theta^*, \phi^*) = \sum_{n=0}^p \sum_{m=-n}^n \Gamma_{(0),n}^m Y_n^m(\theta^*, \phi^*) =: \tilde{\Gamma}(\theta, \phi) = \sum_{n=0}^p \sum_{m=-n}^n \tilde{\Gamma}_n^m Y_n^m(\theta, \phi), \quad (46)$$

where $\tilde{\mathbf{x}}_n^m$ and $\tilde{\Gamma}_n^m$ are given by eq. (12).

This whole procedure is done for all discrete points on the surface in each pseudo time step, and it is summarized in the pseudo-code Algorithm 2.

To test the new reparametrization, we intentionally distort⁶ the grid of an ellipsoid with aspect ratio (1:2) as shown in Fig. 11(a) and let the new procedure run.

The reparametrization is following only a fictitious velocity, so the surfactant distribution should not change but appear the same as in Fig. 11(a) also after the reparametrization (Fig. 11(b)). In Fig. 12 we compare the error in the volume and the area conservations for the two methods of reparametrization, the new angle-reparametrization and the old point-reparametrization. In both cases, the adaptive n_{cutoff} and a *Perfect Low-Pass Filter* are used. We can see the spectral decay of the error for the new reparametrization and, moreover, the dependence/independence from the pseudo-time step τ can clearly be seen (Fig. 12): the error for the *point-reparametrization* is growing with this parameter, whilst for the *angle-reparametrization* it stays fixed and much smaller. This is because, with the *point-reparametrization*, we want to move the points tangential to the surface, but we practically have to deal with a discrete system and then a large pseudo-time step might bring the new point distribution far from the surface, as shown in the sketch of Fig. 10. With the new method, instead, we compute the new point distribution and the new surfactant concentration by evaluating a spherical transform, using the spherical harmonic coefficients $\mathbf{x}_{(0),n}^m$ and $\Gamma_{(0),n}^m$ of the original surface/surfactant concentration, see eqs. (45)–(46). We are basically projecting the new position vector on the surface and computing the corresponding angle parameters;

⁵ The matrix A in (43) is the so-called metric tensor g_{ij} with its inverse g^{ij} and, using enumeration instead of ϕ, θ , we can write

$$\begin{aligned} \mathbf{w} &= \alpha^i \mathbf{e}_i, \\ \alpha^i &= \mathbf{e}^i \cdot \mathbf{w} = (g^{ij} \mathbf{e}_j) \cdot \mathbf{w} = g^{ij} (\mathbf{e}_j \cdot \mathbf{w}), \end{aligned}$$

where $\mathbf{e}^i := g^{ij} \mathbf{e}_j$, \mathbf{e}_j being the normalized vector tangential to the surface [14].

⁶ We apply an artificial tangential velocity given by $\mathbf{v} = 3k \cos(3\theta) \mathbf{t}_\phi + 2k \cos(3\phi) \mathbf{t}_\theta$ until the computational time $T = 3$, with $k = 0.01$.

Algorithm 2 Reparametrization.

Given an initial configuration for the drop surface and for the surfactant concentration, we upsample by a factor U_{rep} ; on this finer grid the initial drop surface and initial surfactant concentration are given by $[\mathbf{x}_0(\theta, \phi), \Gamma_0(\theta, \phi)]$ with spectra $[\mathbf{x}_{(0),n}^m, \Gamma_{(0),n}^m]$. Set $\tilde{\mathbf{x}}(\theta, \phi) = \mathbf{x}_0(\theta, \phi)$ and $\tilde{\mathbf{x}}_n^m = \mathbf{x}_{(0),n}^m$:

```

while ++i < imax do
  • Compute the energy using eq. (37) and adaptive  $n_{cutoff}$  computed through eq. (39);
  • Use the computed energy for obtaining the pseudo-velocity  $\frac{\partial \mathbf{x}}{\partial \tau} = \mathbf{w}(\theta, \phi)$  through eq. (38);
  • Solve system (42) to find the parameter pseudo-velocity  $\alpha = (\frac{\partial \theta}{\partial \tau}, \frac{\partial \phi}{\partial \tau})$ ;
  • Compute the new parameters  $(\theta^*, \phi^*)$  using a forward Euler step;
  • Update the position vector using the initial expansion coefficients, eq. (45);
  • Compute the updated expansion coefficients  $\tilde{\mathbf{x}}_n^m$  via (21);
  • Compute the normal vector and the gradient of the energy (37) corresponding to the new position in order to update  $\mathbf{g}$  via eq. (36);
  if  $\|\mathbf{g}\| < \epsilon$  then break
end if
end while
  • Compute the new surfactant concentration using the initial expansion coefficients, eq. (46);
  • Compute the updated expansion coefficients  $\tilde{\Gamma}_n^m$  via (21).

```

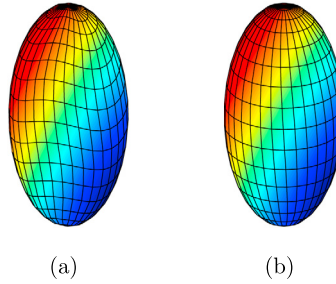


Fig. 11. The distorted ellipsoid with $\Gamma = 2 - \frac{1}{2}x_1 + x_2 + \frac{1}{2}x_3$, (a) pre and (b) after reparametrization. Colors denote the surfactant concentration.

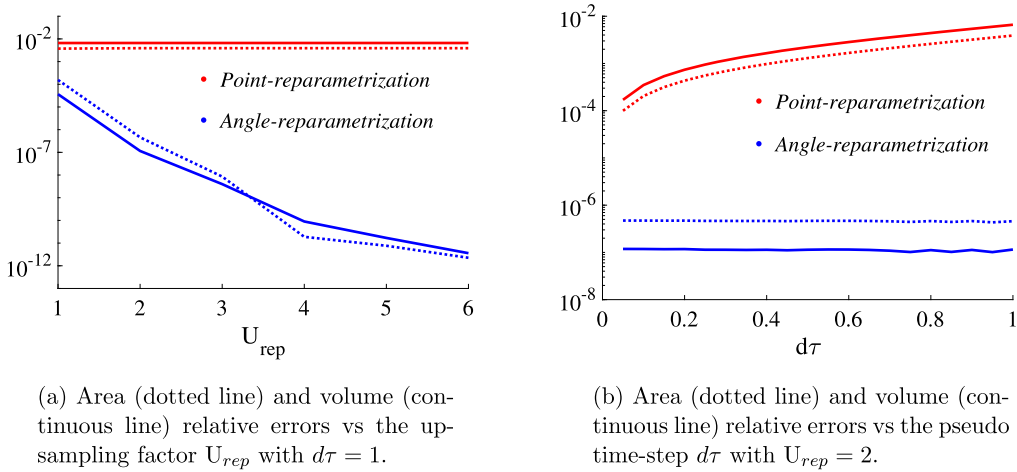


Fig. 12. Comparing the *point-reparametrization* and the new *angle-reparametrization*, $p = 7$, for the test case shown in Fig. 11.

for this reason the size of the pseudo-time step is not a restriction anymore. Note also that the level of the error for the new reparametrization procedure is set by the upsampling rate of the reparametrization U_{rep} . This is shown in the example of Fig. 12: if we compare the level of the error in Fig. 12(b) we can see that it corresponds to the error in Fig. 12(a) for $U_{rep} = 2$.

Finally we can check the surfactant concentration accuracy after the reparametrization using an analytical solution (Fig. 11(b)):

$$\Gamma = 2 - \frac{1}{2}x_1 + x_2 + \frac{1}{2}x_3$$

and we found that the error is very low ($< 10^{-15}$). This is obvious since we are just evaluating a spherical transform for a well-resolved geometry. We checked the reparametrization procedure for different geometries and surfactant distributions and results behave as for the previous case.

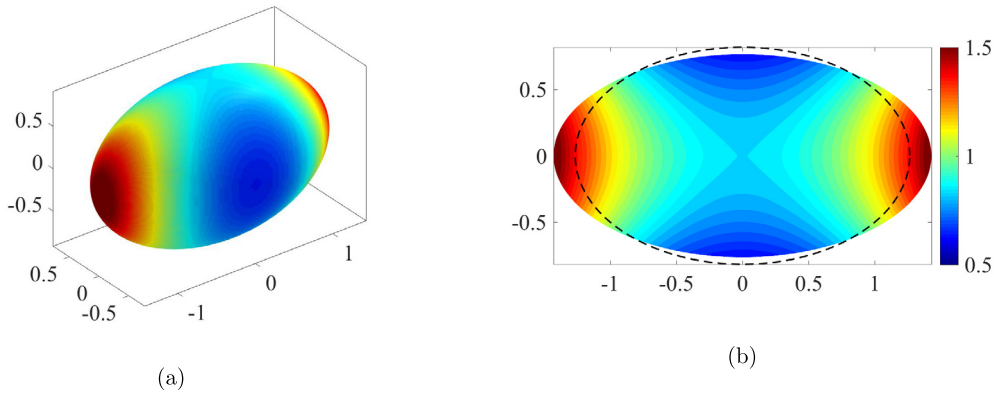


Fig. 13. A single drop in an extensional flow with $E = 0.35$, $Pe = 11.8$, $Ca = 0.1$, $\lambda = 0.093$, $p = 17$. (a) 3D surfactant-covered drop ($x_s = 0.36$) at the steady state; (b) 2D projection to compare clean (black dotted line) and surfactant-covered (colorful) drops at the steady state.

5. Numerical experiments and validation

In this section we will check our numerical method and perform some numerical experiments using the following methods/parameters:

- *Time-stepping scheme*: combination of Midpoint rule (drop) together with the IMEX scheme (surfactant concentration) with adaptivity based on the conservation error (see Algorithm 1) with the tolerance set as $tol = 10^{-5}$;
- *Numerical integration*: for the case of multiple drops, the special quadrature for the nearly singular integration presented in section 2.3 is applied with the following parameters: $\tilde{A} = 5h$, $\tilde{D} = h\sqrt{\tilde{I}}$, $\tilde{U} = 4$ and $\tilde{L} = 8$;
- *Reparametrization*: the angle-reparametrization presented in section 4 is used with the adaptive n_{cutoff} defined in eq. (39) and the following parameters: $P_{cutoff} = 0.2$, $i_{max} = 30$, $\epsilon = 10^{-4}$.

A clean drop case has already been validated in Section 4 comparing our results with the experiments by Bentley and Leal [9], so we proceeded by validating our code with standard tests for the surfactant convection–diffusion equation. In order to make the reader more familiar with the role of each single term acting in eq. (5), we describe the tests below:

1. *Diffusion term*: in this case we do not consider the convective and the stretching term and, starting by a non-constant initial Γ , we can see the effect of the diffusion spreading the surfactant on the whole surface until it reaches a constant concentration, slower or faster depending on the Péclet number.
2. *Stretching term*: we consider the uniform expansion of a spherical drop, radius $R(t)$, uniformly coated with insoluble surfactant concentration $\Gamma(t)$. The Péclet number is set to infinity so that only the stretching term is active (there is only the normal velocity component, so the convection term is zero). In this case we have the analytical solution

$$\Gamma R^2(t) = \Gamma(0),$$

so that $\frac{\partial \Gamma}{\partial t} + 2\frac{\Gamma}{R}\frac{\partial R}{\partial t} = 0$, which is in agreement with equation (5), since the mean curvature of the sphere is $-\frac{1}{R}$ and then the stretching term is exactly $(\nabla_S \cdot \mathbf{n})(\mathbf{u} \cdot \mathbf{n}) = \frac{2}{R}\frac{\partial R}{\partial t}$.

3. *Convective term*: for this case we consider a rotating sphere again with infinite Péclet number. In this case only the tangential velocity is non-zero and the solution is kept constant.

At this point we are able to test the whole system, drop/surfactant for a single or multiple interacting drops.

We start by considering a drop with initial spherical shape subject to a planar extensional flow $\mathbf{u} = (x, -y, 0)$ immersed in a fluid with a different viscosity, $\lambda = 0.093$. The specific value of λ has been set by the experimental results [25] and makes all the terms involved in our equation to be active: when $\lambda \neq 1$ we know that both the single and the double-layer play a fundamental role; moreover, when λ is small and the surfactant coverage is big enough, the Marangoni term becomes significant [8] and so the effect of the surfactant. We compare the behavior of a clean drop, with a surfactant-covered drop with surface-coverage (eq. 6) $x_s = 0.36$, see Fig. 13. We can see that the surfactant acts to lower the surface tension and consequently the drop deforms more. We found for these experiments the deformation numbers (40) $D_{x_s=0} \approx 0.21$ and $D_{x_s=0.36} \approx 0.30$. These results are in good agreement with both the experimental results by Hu and Lips [25] and with the numerical results by Bazhlekova et al. [8] (see Fig. 8 in [8] where both experimental and numerical results are shown). We also performed a convergence test for this example: computing a reference solution ($p = 29$) we look at the error for the drop position and surfactant concentration at a steady state, see Fig. 14. This is a particularly interesting and complicated example to test: it's a time dependent problem, we are looking at a long time horizon and there is a strong tangential flow

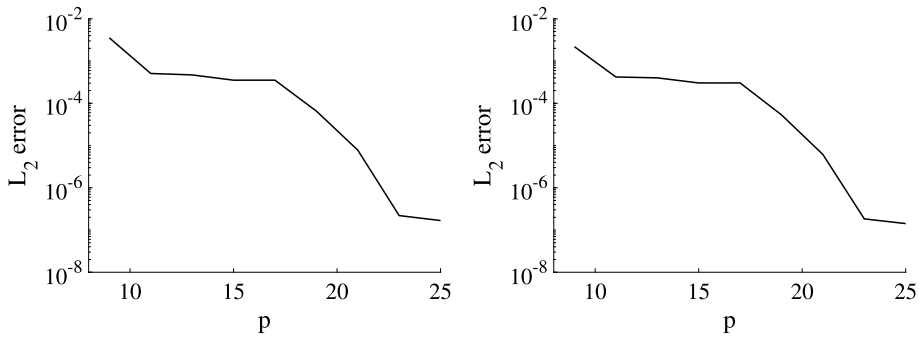


Fig. 14. L_2 norm of the error for the validation test of Fig. 13. The error is computed for the spherical harmonics coefficients vector of the drop position (left) and of the surfactant concentration (right) using a reference solution obtained with $p = 29$.

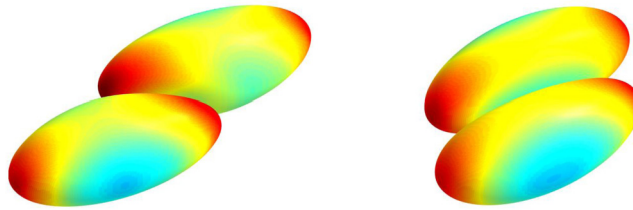


Fig. 15. Two surfactant-covered drops in a shear flow at time $T = 18$. Comparing two different viscosity ratio: $\lambda = 1$ (left) and $\lambda = 2$ (right).

that distorts the point distribution on the drop even when the shape is steady. For this reason, the reparameterization is constantly activated and, since this procedure is not fixed when changing the expansion order p , it could ruin smooth error decay with increasing resolution; this is another reason why looking at the converge plot is so challenging. Nevertheless, we can see the convergence of the error in Fig. 14 where the final flattened part occurs as we are getting close to the finite resolution used to compute the reference solution, and we are already below the set time step tolerance.

Finally, with confidence from the successful comparisons with numerical and experimental results, we proceed with a numerical simulation of two interacting drops. Unfortunately there are no analytical, experimental or numerical results to validate the multiple surfactant covered drops experiment, but we show how our method can handle also very close interactions, how the deformation is affected by the presence of the surfactant and by the viscosity ratio λ . In this experiment two drops are immersed in a shear flow and pushed against each other reaching a very small distance (Fig. 15), so that the special quadrature for the nearly-singular integrals becomes fundamental. In Fig. 16 we show 2D projections of the drops to compare the clean drops with the surfactant-covered ones at different time-steps for two different values of λ . We can see how the surfactant acts lowering the surface tension and then making the drops deform more as compared to the clean case. The surfactant concentration is higher at the tips and this non-uniform distribution induces a strong Marangoni force. In particular we observe that for the surfactant covered drops, the minimum distance reached is never less than 0.16 for the case $\lambda = 1$ and 0.15 when $\lambda = 2$. When considering the clean drops, due to the smaller deformation, the minimum distance reached is instead 0.058 and 0.056 respectively for $\lambda = 1, 2$ (see Fig. 17) which correspond approximately to $0.25h$ that means that the special quadrature for the nearly-singular integral is absolutely needed as shown in Fig. 3. In Fig. 16 we compare the evolution of the drops at different times and we can observe how the higher viscosity yields a slower deformation. For these simulations the physical parameters used are the following: $\lambda = 1, 2$, $Ca = 0.2$, $Pe = 200$, $E = 0.5$, $x_s = 0.6$. We used $p = 13$ combined with an adaptive upsampling and reparametrization. Note that, even using such a small number of points, we obtain an error at the final time $T = 50$ which is less than 0.2% in the volume conservation and than 0.3% for the surfactant conservation for all cases presented. The maximum number of iterations allowed for the reparametrization is set as $i_{max} = 30$, but in practice we never need so many iterations since we are able to use large pseudo-timesteps as shown in Section 4.

6. Conclusions and future work

In this paper, we have presented a numerical method based on a boundary integral formulation for 3D surfactant covered drops. We have showed how the method can accurately simulate multiple drops immersed in a fluid with different viscosity ($\lambda \neq 1$) also as very close interactions occur thanks to special quadrature methods for singular and nearly singular integrals.

We presented a new reparameterization method able to maintain a good quality of the surface representation, a crucial point when dealing with strong deformations as in our case. This new procedure can deal with large pseudo-timesteps and can therefore ensure fast convergence, at the same time achieving spectral accuracy of the drop volumes/areas. In addition, it provides a way to redefine the representation of any surface quantity, in our case the surfactant concentration, such that

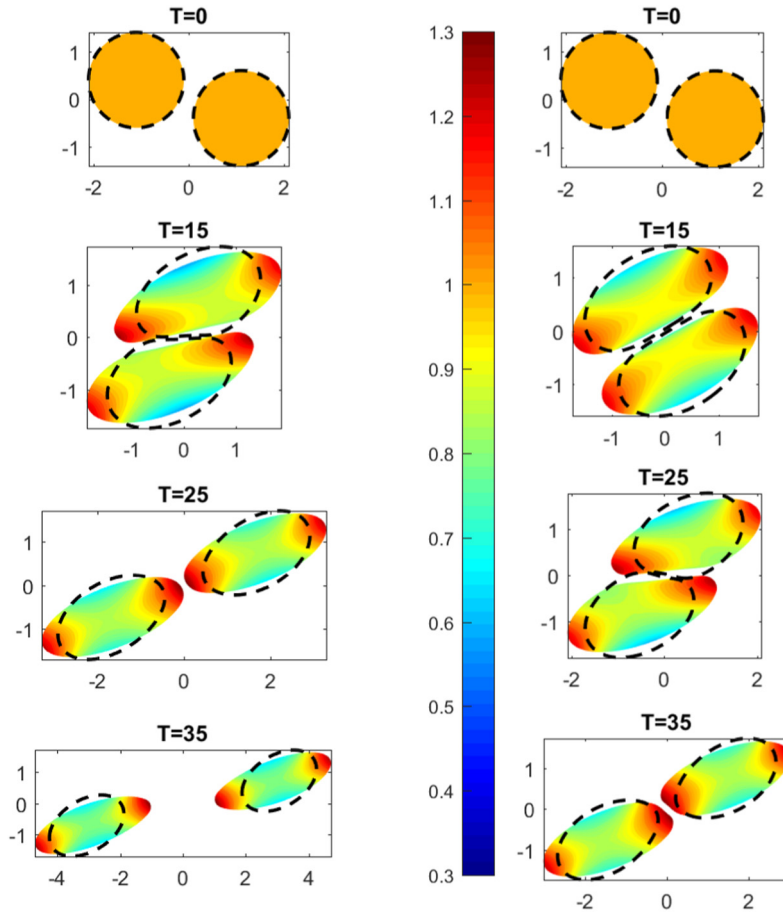


Fig. 16. Projections of two surfactant-covered drops interacting in a shear flow; the colors denote the surfactant concentration, the dotted line denote a clean drop. Comparing two different viscosity ratio: $\lambda = 1$ (left column) and $\lambda = 2$ (right column).

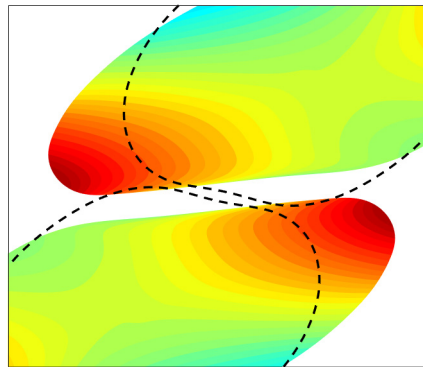


Fig. 17. Zoom of the interaction between two drops for $\lambda = 2$, $T = 25$. The colors denote the surfactant concentration, the dotted line denote the contour of a clean drop.

it corresponds to the new drop discretization while conserving the surface quantity (pointwise error of the surfactant) to spectral accuracy.

Since the discretization is based on a boundary integral equation, only the surfaces of the drops must be discretized as compared to the full volume, and moreover with the representations based on a spherical harmonics expansion the number of unknowns can be kept low while still giving an excellent representation of the surfaces and of any quantities that live on the drops. This means that the system sizes for the Stokes solvers are small, but the matrices are however dense. The integral equation is of second kind, and yields a well conditioned system for which the condition number stays constant with an increased resolution on the drop surfaces, even though it depends on the geometry of the problem. This implicates

that as the linear system is solved iteratively with GMRES, the number of iterations does not grow with increased resolution and the computational cost is $O(n^2)$, with $n = N(p+1)(p+2)$. This cost can be further reduced by using a fast summation method to evaluate the matrix-vector multiply to $O(n)$ or $O(n \log n)$. The fast multipole method [52] is one alternative, others include the FFT based Ewald methods that has been developed for periodic [32], [5] and recently also for free-space [1] settings. In the simulations presented in this paper, we have not used these methods, but it will become necessary as we want to consider more drops in one simulation.

We studied and compared different combinations of time-stepping schemes for the drop-surfactant system, with the design criteria to minimize the number of solvers of the Stokes equations relative to the achieved accuracy, since this is the computationally most costly part. The final choice (Midpoint rule with IMEX 2nd order) is adaptive based on the estimated accuracy for both the drop and surfactant evolution, ensuring to keep the error below a given tolerance. This method treats the diffusive term in the surfactant equation implicitly, reducing the CFL condition to first order. This however requires a system to be solved, which we do with GMRES. To accelerate the convergence of the iterations, we introduce a preconditioner based on analytical properties of the spherical harmonics.

This is only one of the advantages of using a spherical harmonics representation: a Galerkin formulation (Section 1.2) results to be cheaper than a discrete solver for the physical variables; in the reparametrization procedure the spherical harmonics representation can ensure spectral decay of the error and no strict pseudo-time restrictions. Also when computing singular and nearly-singular integrals, the spherical harmonics representation plays a fundamental role: in the first case (Section 2.2) we use analytical expressions for the rotation of the spherical harmonics coefficients (Appendix B), and when computing the interpolation for the nearly-singular quadratures (Section 2.3), the on-surface value is based on a spherical harmonics interpolation. When two or more drops are getting close enough that the special quadrature evaluation is needed, the evaluation of the nearly singular integrals become expensive. Since no error estimates are available to guide parameter selection in the special quadrature method, choices that yields unnecessarily expensive computations might be made to ensure sufficient accuracy. In [3] af Klinteberg and Tornberg developed a quadrature method denoted Quadrature by Expansion (QBX) [30] for the case of spheroidal rigid particles in Stokes flow. The known geometry of the rigid particles allows for precomputations that makes the method very efficient. For deformable drops, such precomputations are not possible. In [2] af Klinteberg and Tornberg developed an adaptive QBX method (AQBX) in two dimensions. Given a user specified error tolerance, parameters are selected on the fly to meet this tolerance, using error estimates derived in [4].

If error estimates such as those in [4,2] would be available in three dimensions, they could be used to determine the accuracy that the quadrature method with a specific resolution yields at a given target point. Hence, given an error tolerance, they could also predict what upsampling is required to achieve that accuracy. This could then be used to determine the parameters \tilde{A} and \tilde{U} introduced in section 2.3. Further analysis is however needed to ensure that the error in the interpolation procedure in the nearest region (where it is unfeasible with plain upsampling) can be controlled and optimal parameters selected. An alternative route is to use the idea of target specific QBX (TSQBX) as introduced in [44], in the nearest region, which would build on a generalization of the methodology in [2]. Both these approaches do however need rather precise error estimates, and our first aim will be to extend the error analysis to three dimensions. Only then can we pursue the goal to design an algorithm that automatically selects parameters to minimize the cost of the integral evaluation, while maintaining errors below a set tolerance.

Acknowledgements

This work has been supported by the Knut and Alice Wallenberg Foundation under grant no KAW 2013.0339 and is gratefully acknowledged.

We thank Zydrunas Gimbutas and Shravan Veerapaneni for sharing their fast code for the rotation of the spherical harmonics expansions [21] which has been used in the present work.

Appendix A. Derivatives of spherical harmonics

For convenience, we will use the normalized associated Legendre functions which will be denoted by $\tilde{P}_n^m(x)$:

$$\tilde{P}_n^m(x) = \sqrt{\frac{2n+1}{4\pi} \frac{(n-m)!}{(n+m)!}} P_n^m(x). \quad (\text{A.1})$$

It follows that:

$$\begin{aligned} \tilde{P}_n^{-m}(x) &= \sqrt{\frac{2n+1}{4\pi} \frac{(n+m)!}{(n-m)!}} P_n^{-m}(x) \\ &= \sqrt{\frac{2n+1}{4\pi} \frac{(n+m)!}{(n-m)!}} (-1)^m \frac{(n-m)!}{(n+m)!} P_n^m(x) \\ &= (-1)^m \sqrt{\frac{2n+1}{4\pi} \frac{(n-m)!}{(n+m)!}} P_n^m(x) = (-1)^m \tilde{P}_n^m(x), \end{aligned} \quad (\text{A.2})$$

so that

$$f(\theta, \phi) = \sum_{n=0}^p \sum_{m=-n}^n f_n^m Y_n^m(\theta, \phi) = \sum_{n=0}^p \sum_{m=-n}^n f_n^m \tilde{P}_n^m(\cos(\theta)) e^{im\phi}. \quad (\text{A.3})$$

To compute the normalized associated Legendre functions, we can use the following recursive relations ($m \geq 0$):

$$\begin{cases} \tilde{P}_0^0 &= \sqrt{\frac{1}{4\pi}}, \\ \tilde{P}_m^m &= -c_m \sqrt{1-x^2} \tilde{P}_{m-1}^{m-1}, \\ \tilde{P}_{m+1}^m &= \sqrt{2m+3} x \tilde{P}_m^m, \\ \tilde{P}_n^m &= a_n^m (x \tilde{P}_{n-1}^m + b_n^m \tilde{P}_{n-2}^m) \end{cases}$$

where $a_n^m = \sqrt{\frac{4n^2-1}{n^2-m^2}}$, $b_n^m = -\sqrt{\frac{(n-1)^2-m^2}{4(n-1)^2-1}}$, $c_n^m = \sqrt{1 + \frac{1}{2m}}$.

The k -th derivatives of f are then computed by:

$$\frac{\partial^k f}{\partial \phi^k}(\theta, \phi) = \sum_{n=0}^p \sum_{m=-n}^n (im)^k f_n^m Y_n^m(\theta, \phi) \quad (\text{A.4})$$

$$\frac{\partial^k f}{\partial \theta^k}(\theta, \phi) = \sum_{n=0}^p \sum_{m=-n}^n f_n^m \frac{\partial^k}{\partial \theta^k} \tilde{P}_n^m(\cos \theta) e^{im\phi} \quad (\text{A.5})$$

where we apply recursion formulas for computing the Associated Legendre Functions derivatives. For $k = 1, 2$ we obtain:

$$\begin{aligned} \frac{d}{d\theta} \tilde{P}_n^m(\cos \theta) &= \alpha_n^m \tilde{P}_n^{m+1}(\cos \theta) + m \cot \theta \tilde{P}_n^m(\cos \theta) \\ &= -\sqrt{d_n^m} \tilde{P}_n^{m-1}(\cos \theta) - m \cot \theta \tilde{P}_n^m(\cos \theta) \end{aligned} \quad (\text{A.6})$$

$$\begin{aligned} \frac{d^2}{d\theta^2} \tilde{P}_n^m(\cos \theta) &= \alpha_n^m \alpha_n^{m-1} \tilde{P}_n^{m+2}(\cos \theta) + \alpha_n^m (2m+1) \cot \theta \tilde{P}_n^{m+1}(\cos \theta) - m^2 \tilde{P}_n^m(\cos \theta) \\ &= \sqrt{d_n^m} \tilde{D}_n^{m+1}(\cos \theta) - m(1 + \cot^2 \theta) \tilde{P}_n^m(\cos \theta) + m \cot \theta \tilde{D}_n^m(\cos \theta) \\ &= \sqrt{d_n^m} \cot \theta \tilde{P}_n^{m-1}(\cos \theta) + (-d_n^m + m + m(1+m) \cot^2 \theta) \tilde{P}_n^m(\cos \theta) \end{aligned} \quad (\text{A.7})$$

where $d_n = (n+m)(n-m+1)$, $\alpha_n^m = \sqrt{(n-m)(n+m+1)}$.

Appendix B. Rotation of spherical harmonics

In order to compute singular integrals, we need to rotate the pole of the spherical harmonics expansion into a general grid location (β, α) . In the rotated system, the function f defined in (13) can be expressed as ([21], [20], [13]):

$$f(\theta', \phi') = \sum_{n=0}^p \sum_{m'=-n}^n f_n^{m'}(\alpha, \beta, \gamma) Y_n^{m'}(\theta', \phi') \quad (\text{B.1})$$

where (θ', ϕ') denote the new coordinates,

$$f_n^{m'}(\alpha, \beta, \gamma) = \sum_{m=-n}^n D_n^{m',m}(\alpha, \beta, \gamma) f_n^m \quad (\text{B.2})$$

and the standard Euler angles (α, β, γ) define the rotation using the $z-y-z$ convention, meaning that we first rotate by an angle α respect to the z -axis, then by an angle β respect to the new y -axis and then again by an angle γ respect to the new z -axis. The coefficients of the transformation are given by [54]:

$$D_n^{m',m}(\alpha, \beta, \gamma) = e^{im'\gamma} d_n^{m',m}(\beta) e^{im\alpha}, \quad (\text{B.3})$$

where

$$d_n^{m',m}(\beta) = (-1)^{m'-m} [(n+m')!(n-m')!(n+m)!(n-m)!]^{1/2} S_n^{m',m} \quad (\text{B.4})$$

with

$$S_n^{m',m}(\beta) = \sum_{s=\max(0, m-m')}^{\min(n+m, n-m')} (-1)^s \frac{(\cos \frac{\beta}{2})^{2(n-s)+m-m'} (\sin \frac{\beta}{2})^{2s-m+m'}}{(n+m-s)! s! (m'-m+s)! (n-m'-s)!}. \quad (\text{B.5})$$

References

- [1] L. af Klinteberg, D. Saffar Shamshirgar, A.-K. Tornberg, Fast Ewald summation for free-space Stokes potentials, *Res. Math. Sci.* 4 (1) (2017).
- [2] L. af Klinteberg, A.-K. Tornberg, Adaptive quadrature by expansion for layer potential evaluation in two dimensions, arXiv:1704.02219 [math.NA], 2017.
- [3] L. af Klinteberg, A.-K. Tornberg, A fast integral equation method for solid particles in viscous flow using quadrature by expansion, *J. Comput. Phys.* 326 (2016) 420–445.
- [4] L. af Klinteberg, A.-K. Tornberg, Error estimation for quadrature by expansion in layer potential evaluation, *Adv. Comput. Math.* 43 (1) (2017) 195–234.
- [5] L. af Klinteberg, A.-K. Tornberg, Fast Ewald summation for Stokesian particle suspensions, *Int. J. Numer. Methods Fluids* 76 (10) (2014) 669–698.
- [6] U.M. Ascher, S.J. Ruuth, E.J. Spiteri, Implicit-explicit Runge–Kutta methods for time-dependent partial differential equations, *Appl. Numer. Math.* 25 (2–3) (1997) 151–167.
- [7] K. Atkinson, W. Han, *Spherical Harmonics and Approximations on the Unit Sphere: An Introduction*, Lecture Notes in Mathematics, vol. 2044, Springer, 2012.
- [8] I.B. Bazhlekova, P.D. Anderson, H.E.H. Meijer, Numerical investigation of the effect of insoluble surfactants on drop deformation and breakup in simple shear flow, *J. Colloid Interface Sci.* 298 (2006) 269–394.
- [9] B.J. Bentley, L.G. Leal, An experimental investigation of drop deformation and breakup in steady, two-dimensional linear flows, *J. Fluid Mech.* 167 (1986) 241–283.
- [10] J.P. Boyd, *Chebyshev and Fourier Spectral Methods*, Dover Publications Inc., 1999.
- [11] J. Bremer, Z. Gimbutas, A Nyström method for weakly singular integral operators on surfaces, *J. Comput. Phys.* 231 (14) (2012) 4885–4903.
- [12] J. Bremer, Z. Gimbutas, On the numerical evaluation of the singular integrals of scattering theory, *J. Comput. Phys.* 251 (2013) 327–343.
- [13] G. Burel, H. Henocq, Determination of the orientation of 3D objects using spherical harmonics, *Graph. Models Image Process.* 57 (5) (1995) 400–408.
- [14] I. Chavel, *Riemannian Geometry: A Modern Introduction*, Cambridge University Press, 1995.
- [15] A.T. Chwang, T.Y.-T. Wu, Hydromechanics of low-Reynolds-number flow. Part 2. Singularity method for Stokes flows, *J. Fluid Mech.* 67 (4) (1975) 787–815.
- [16] J.E. Dennis Jr., R.B. Schnabel, *Numerical Methods for Unconstrained Optimization and Nonlinear Equations*, Classics in Applied Mathematics, SIAM, 1996.
- [17] P. Dimitrakopoulos, Interfacial dynamics in Stokes flow via a three-dimensional fully-implicit interfacial spectral boundary element algorithm, *J. Comput. Phys.* 225 (2007) 408–426.
- [18] K. Feigl, D. Megias-Alguacil, P. Fischer, E.J. Windhab, Simulation and experiments of droplet deformation and orientation in simple shear flow with surfactant, *Chem. Eng. Sci.* 62 (2007) 3242–3258.
- [19] M. Ganesh, I.G. Graham, A high-order algorithm for obstacle scattering in three dimensions, *J. Comput. Phys.* 198 (2004) 211–242.
- [20] Z. Gimbutas, L. Greengard, A fast and stable method for rotating spherical harmonic expansions, *J. Comput. Phys.* 228 (2009) 5621–5627.
- [21] Z. Gimbutas, S.K. Veerapaneni, A fast algorithm for spherical grid rotations and its application to singular quadrature, *SIAM J. Sci. Comput.* 35 (6) (2013) A2738–A2751.
- [22] I.G. Graham, I.H. Sloan, Fully discrete spectral boundary integral methods for Helmholtz problems on smooth closed surfaces in \mathbb{R}^3 , *Numer. Math.* 92 (2002) 289–323.
- [23] E. Hairer, S.P. Norsett, G. Wanner, *Solving Ordinary Differential Equations I: Nonstiff Problems*, Springer, Berlin, 1993.
- [24] P. Hansbo, M.G. Larson, S. Zahedi, A cut finite element method for a Stokes interface problem, *Appl. Numer. Math.* 85 (2014) 90–114.
- [25] Y.T. Hu, A. Lips, Estimating surfactant surface coverage and decomposing its effect on drop deformation, *Phys. Rev. Lett.* 91 (2003).
- [26] G.B. Jeffery, The motion of ellipsoidal particles immersed in a viscous fluid, *Proc. R. Soc. A, Math. Phys. Eng. Sci.* 102 (715) (1922) 161–179.
- [27] H.N. Joensson, M.L. Samuels, E.R. Brouzes, M. Medkova, M. Uhle, D.R. Link, H.A. Svahn, Detection and analysis of cell surface biomarkers, *Angew. Chem., Int. Ed. Engl.* 48 (14) (2009) 2518–2521.
- [28] S. Khatri, A.-K. Tornberg, A numerical method for two phase flows with insoluble surfactants, *Comput. Fluids* 49 (1) (2011) 150–165.
- [29] S. Khatri, A.-K. Tornberg, An embedded boundary method for soluble surfactants with interface tracking for two-phase flows, *J. Comput. Phys.* 256 (2014) 768–790.
- [30] A. Klöckner, A. Barnett, L. Greengard, M. O’Neil, Quadrature by expansion: a new method for the evaluation of layer potentials, *J. Comput. Phys.* 252 (2013) 332–349.
- [31] X. Li, C. Pozrikidis, The effect of surfactants on drop deformation and on the rheology of dilute emulsions in Stokes flow, *J. Fluid Mech.* 341 (1997) 165–194.
- [32] D. Lindbo, A.-K. Tornberg, Spectrally accurate fast summation for periodic Stokes potentials, *J. Comput. Phys.* 229 (23) (2010) 8994–9010.
- [33] M. Minion, Semi-implicit spectral deferred correction methods for ordinary differential equations, *Commun. Math. Sci.* 1 (3) (2003) 471–500.
- [34] M.J. Mohlenkamp, A fast transform for spherical harmonics, *J. Fourier Anal. Appl.* 5 (2) (1999) 159–184.
- [35] M. Muradoglu, G. Tryggvason, A front-tracking method for computation of interfacial flows with soluble surfactants, *J. Comput. Phys.* 227 (2008) 2238–2262.
- [36] S.A. Orszag, Fourier series on spheres, *Mon. Weather Rev.* 102 (1974) 56–75.
- [37] Y. Pawar, K.J. Stebe, Marangoni effects on drop deformation in an extensional flow: the role of surfactant physical chemistry. I. Insoluble surfactants, *Phys. Fluids* 8 (1996) 1738–1751.
- [38] C. Pozrikidis, *Boundary Integral and Singularity Methods for Linearized Viscous Flow*, Cambridge Texts in Applied Mathematics, 1992.
- [39] B. Quaife, G. Biros, Adaptive time stepping for vesicle suspensions, *J. Comput. Phys.* 306 (2016) 478–499.
- [40] A. Quarteroni, R. Sacco, F. Saleri, *Numerical Mathematics: Numerical Solution of Ordinary Differential Equations*, Springer, Berlin, Heidelberg, 2007.
- [41] A. Rahimian, S.K. Veerapaneni, D. Zorin, G. Biros, Boundary integral method for the flow of vesicles with viscosity contrast in three dimensions, *J. Comput. Phys.* 298 (2015) 766–786.
- [42] N. Schaeffer, Efficient spherical harmonic transforms aimed at pseudospectral numerical simulations, *Geochem. Geophys. Geosyst.* 14 (2013) 751–758.
- [43] N. Shembekar, C. Chaipan, R. Utharala, C.A. Merten, Droplet-based microfluidics in drug discovery, transcriptomics and high-throughput molecular genetics, *Lab Chip* 16 (2016) 1314.
- [44] M. Siegel, A.-K. Tornberg, A local target specific quadrature by expansion method for evaluation of layer potentials in 3D, arXiv:1707.04524 [math.NA], 2017.
- [45] Y. Skhiri, et al., Dynamics of molecular transport by surfactants in emulsions, *Soft Matter* 8 (2012) 10618–10627.
- [46] H.A. Stone, A simple derivation of the time-dependent convective-diffusion equation for surfactant transport along a deforming interface, *Phys. Fluids A, Fluid Dyn.* 2 (1990) 111.
- [47] H.A. Stone, Dynamics of drop deformation and breakup in viscous fluids, *Annu. Rev. Fluid Mech.* 26 (1994) 65.
- [48] H.A. Stone, L.G. Leal, The effects of surfactants on drop deformation and breakup, *J. Fluid Mech.* 220 (1990) 161–186.
- [49] S.Y. Teh, R. Lin, L.H. Hungand, A.P. Lee, Droplet microfluidics, *Lab Chip* 8 (2) (2008) 198–220.
- [50] K.E. Teigen, P. Song, J. Lowengrub, A. Voigt, A diffuse-interface method for two-phase flows with soluble surfactants, *J. Comput. Phys.* 230 (2011) 375–393.

- [51] S. Tlupova, J.T. Beale, Nearly singular integrals in 3D Stokes flow, *Commun. Comput. Phys.* 14 (5) (2013) 1207–1227.
- [52] A.-K. Tornberg, L. Greengard, A fast multipole method for the three-dimensional Stokes equations, *J. Comput. Phys.* 227 (2008) 1613–1619.
- [53] S.K. Veerapaneni, A. Rahimian, G. Biros, D. Zorin, A fast algorithm for simulating vesicle flows in three dimensions, *J. Comput. Phys.* 230 (2011) 5610–5634.
- [54] E.P. Wigner, *Group Theory and Its Application to the Quantum Mechanics of Atomic Spectra*, Academic Press, 1959.
- [55] M. Wörner, Numerical modeling of multiphase flows in microfluidics and micro process engineering: a review of methods and applications, *Microfluid. Nanofluid.* 12 (2012) 841–886.
- [56] K. Xu, M.R. Booty, M. Siegel, Analytical and computational methods for two-phase flow with soluble surfactant, *SIAM J. Appl. Math.* 73 (1) (2013) 523–548.
- [57] J.-J. Xu, Z. Li, J. Lowengrub, H. Zhao, A level-set method for interfacial flows with surfactant, *J. Comput. Phys.* 212 (2) (2006) 590–616.
- [58] L. Ying, G. Biros, D. Zorin, A high-order 3D boundary integral equation solver for elliptic PDEs in smooth domains, *J. Comput. Phys.* 219 (2005) 247–275.
- [59] S. Yon, C. Pozrikidis, A finite-volume/boundary-element method for flow past interfaces in the presence of surfactants, with application to shear flow past a viscous drop, *Comput. Fluids* 27 (8) (1998) 879–902.
- [60] Z. Zapryanov, S. Tabakova, *Dynamics of Bubbles, Drops and Rigid Particles*, Springer Science + Business Media, Dordrecht, 1999.
- [61] H. Zhao, A.H. Isfahani, L.N. Olson, J.B. Freund, A spectral boundary integral method for flowing blood cells, *J. Comput. Phys.* 229 (10) (2010) 3726–3744.
- [62] A.Z. Zinchenko, M.A. Rother, R.H. Davis, A novel boundary-integral algorithm for viscous interaction of deformable drops, *Phys. Fluids* 9 (1997) 1493.